Astronomy & Astrophysics manuscript no. output
January 29, 2025

Euclid Quick Data Release (Q1)

The *Euclid* view on *Planck* galaxy protoclusters candidates: probing the highest sites of star-formation at cosmic noon ?

Euclid Collaboration: H. Dole*[1], T. Dusserre[1], F. Sarron[2], G. Castignani[3], N. Ramos-Chernenko[4], N. Aghanim[1], A. Garic[1], I.-E. Mellouki[1], N. Dagoneau[5], O. Chapuis[6], B. Frye[7], M. Polletta[8,9], H. Dannerbauer[4], M. Langer[1], L. Maurin[1], E. Soubrié[1], and ET AL., INCLUDING: D. Scott[10]

(Affiliations can be found after the references)

January 29, 2025

ABSTRACT

In this pilot study, we search for galaxy protoclusters at redshifts $z > 1.5$ in the first data of the *Euclid* survey, Q1, released to the public and covering about 50 deg^2. We make use of the catalogues delivered by the *Euclid* science ground segment (SGS), especially the positions, photometry, the photometric redshifts, and the derived physical parameters. After a galaxy selection on the $H_{\rm E}$ magnitude and on the photometric redshift quality, we search for protoclusters in the fields using the DETECTIFz algorithm, an overdensity finder based on Delaunay tessellation that uses photometric redshifts probability distribution through Monte Carlo simulations. We conduct a blind search and found 81 overdensities. At the positions of 12 previously known *Planck* high star-forming galaxy protoclusters candidates situated in the Q1 footprint, we find eleven *Euclid* protocluster counterparts of *Planck* sources. Two of them have a signal-to-noise ratio greater than 4.75 and lie at photometric redshifts $z_{\rm ph} = 1.48^{+0.3}_{-0.12}$ and $z_{\rm ph} = 1.62^{+0.23}_{-0.26}$. The five weaker detections lie in the redshift range $z_{\rm ph} = 1.45$–1.90. We provide in addition a list of four tentative detections $z_{\rm ph} = 1.45$–2.70. These eleven *Euclid* protoclusters coincide with *Planck* candidates, and some have *Herschel* counterparts. The seven best protocluster detections have all been confirmed by at least one other independent protocluster detection algorithms, and two algorithms for some. After studying the colours, the derived stellar masses (lower limits) and star-formation rates of the seven detected protoclusters, we estimate their halo masses. We question whether we are witnessing these protoclusters in the "dying protocluster phase" (or the "protocluster swan song"), as their high star-formation rates are likely due to their last unsustainable starburst (or star formation event) before transitioning and maturing to groups or clusters of galaxies. Some galaxy members are found to lie above the main sequence of galaxies (star-formation rate vs. stellar mass). These *Planck* and *Euclid* protoclusters occupy a sweet spot in the dark matter halo mass / redshift plane around (12.0–13.3, 1.5–2): in this locus, haloes of forming galaxy clusters are expected to experience a transition between cold flows with no shock heating throughout the halo to shock heating in the halo. Finally, we empirically update the potentialities of galaxy protocluster discoveries at redshift up to $z \sim 3$ (wide survey) and $z \sim 5.5$ (deep survey) with *Euclid* for the coming data release 1 (DR1).

Key words. Methods: statistical; Surveys; Cosmology: observations; large-scale structure of Universe; Galaxies: clusters: general; Galaxies: star formation

1. Introduction

Large-scale structures of the Universe form hierarchically via the gravitational collapse of initial density perturbations. They are distributed in the form of a complex cosmic web network of filaments, walls, voids, and nodes. The most massive nodes, at the intersection of filaments, are the sites of clusters of galaxies and of their high-redshift progenitors, also called protoclusters (see Overzier 2016; Alberts & Noble 2022; Remus et al. 2023, for a definition of protoclusters). Understanding how the present largest gravitationally bound structures, namely clusters of galaxies, transitioned from an early protocluster stage is a key question to fully understand the matter assembly in the Universe.

Protoclusters are pivotal to understand structure formation as they represent the environments primarily driving the properties of their descendant clusters, both in terms of the mechanisms controlling the evolution galaxy members and in terms of the gas heating processes (see Alberts & Noble 2022, for a recent review). In this context, a particularly crucial but still not elucidated mechanism is quenching (Martig et al. 2009; Schawinski et al. 2014), which describes the transition from star-forming to quiescent galaxies. It marks the end of the so-called Cosmic Noon, at $z \sim 2$–4, which represents the peak epoch for the formation of galaxies and their assembly in clusters (Madau & Dickinson 2014). As such, protoclusters seem to be the best witnesses of this transition and as such their observation in the submillimetre (submm) and infrared (IR) domains offers great opportunities to not only to detect them but also to study star formation and quenching processes at Cosmic Noon. Based on the assumption that important episodes of star formation occurred in protoclusters, several approaches have been proposed to capture this epoch such as the search of overdensities of Hα and Lyα emitters (Steidel et al. 2000; Shi et al. 2019; Koyama et al. 2013) or of dusty star forming galaxies and submm galaxies (Chapman et al. 2009; Clements et al. 2014; Miller et al. 2018; Koyama et al. 2021; Polletta et al. 2021; Gómez-Guijarro et al. 2018; Kneissl et al. 2019; Wang et al. 2016; Ivison et al. 2012; Kubo et al. 2015; Casey et al. 2015; Coogan et al. 2018; Oteo et al. 2018; Calvi et al. 2021; Rotermund et al. 2021; Tadaki et al. 2019; Emonts et al. 2019; Hill et al. 2024). In the same spirit, the largest catalogue of candidate protoclusters (Planck Collab-

* e-mail: Herve.Dole@universite-paris-saclay.fr

Table 1. *Planck* protocluster candidates located in the *Euclid* deep fields Q1 footprint. Columns are: *Euclid* field name; *Planck* field name; *Planck* ID (in the official high-zz source catalog of Planck Collaboration et al. (2016); RA and Dec; and the MER tile number. We mention in the footnote (a) the fields where *Herschel* data are available.

Euclid Deep Field	*Planck* field name	*Planck* ID	RA	Dec	MER tile number
EDF-F	G221.09-54.59[a]	1904	52.6798	−26.4142	102 046 112
EDF-F	G222.05-54.24[a]	1399	53.1806	−26.9014	102 045 467
EDF-F	G222.75-55.98[a]	108	51.3123	−27.5725	102 044 821
EDF-F	G223.18-54.86[a]	2151	52.606	−27.6495	102 044 824
EDF-F	G224.36-53.19[a]	1643	54.5941	−28.0819	102 044 188
EDF-S	G257.45-49.50	320	57.4918	−48.767	102 020 530
EDF-S	G252.47-48.60	600	59.8577	−45.7809	102 023 474
EDF-S	G254.74-47.64[a]	1308	60.8251	−47.4485	102 021 984
EDF-S	G257.13-49.16	1442	58.0698	−48.6542	102 021 010
EDF-S	G254.49-47.73	1494	60.738	−47.2715	102 021 984
EDF-S	G257.71-47.99	1926	59.6462	−49.3164	102 020 059
EDF-S	G257.01-45.18	1975	64.0252	−49.4534	102 020 065
EDF-N	–	–	–	–	–

Pas de Z ?

Notes. [(a)] *Herschel*/SPIRE observations are available and come from: Oliver et al. (2012) in EDF-F and Planck Collaboration et al. (2015b) in EDF-S.

oration et al. 2016) was constructed from the *Planck*[1] all-sky survey by colour-selecting in the submm overluminous regions likely to be associated with star-forming dusty galaxies.

Since the first discoveries of high-redshift clusters and protoclusters and during the last decades (Euclid Collaboration et al. 2025, and references on protocluster detections therein), an increasingly large number of protoclusters were detected significantly enriching the samples of sources needed to decipher the steps by which clusters grow, assemble matter, and shape the properties of their member galaxies across time. Detection and follow-up confirmation of protoclusters were conducted in multiple wavelengths from the radio to the optical. Given their rarity, their number is still small and it is only via large surveys conducted in these wavelengths that the observational situation is expected to drastically change. The large number of candidate protoclusters detected in *Planck* (Planck Collaboration et al. 2016) illustrates the advantage of surveying the whole sky to increase the source statistics, with the caveat that one has to use appropriate physical tracers and detection techniques of protoclusters, in order to reduce contamination by false detections. In this context, stage III (Albrecht et al. 2006) wide galaxy surveys such as the Hyper Suprime-Cam Strategic Survey Program (Aihara et al. 2018) already show that blind detection of more than a hundred protocluster candidates at $z \sim 4$ is possible. Undoubtedly, stage IV surveys such as *Euclid* (Euclid Collaboration: Mellier et al. 2024) , *Vera Rubin*/LSST[2], or *Nancy Roman*[3] covering about a third of the sky will offer unique possibilities to observe high-redshift galaxies and identify tens of thousands of overdense regions that could be associated with distant clusters and/or protoclusters (e.g. Euclid Collaboration et al. 2025).

In this study, we showcase the capability of the *Euclid* (Euclid Collaboration: Mellier et al. 2024) survey to detect protoclusters. We do so by investigating the counterparts in the first *Euclid* data, Q1 (Aussel et al. 2025; Euclid Quick Release Q1 2025) of protocluster candidates already detected in the *Planck* (Planck Collaboration et al. 2016). This pilot study hence provides a first assessment of the *Planck-Euclid* synergy to probe star-forming galaxy protoclusters at Cosmic Noon.

The article starts, in Sect. 2, with the description of the *Euclid* and *Planck* observations used in the study. In Sect. 3, we describe the methods used to detect protoclusters in the *Euclid* data, while in Sect. 4 we highlight the *Euclid* protocluster detections as counterparts of *Planck* protocluster candidates and explore their physical parameters. We discuss in Sect. 5 our findings, in particular the protocluster nature of our detection and their evolutionary state. In Sect. 6 we provide empirical predictions on the redshift range probed by future *Euclid* protocluster detections. Finally, we conclude in Sect. 7 and review what this pilot study raises as open questions. In the following, we use AB magnitudes, and the *Planck* 2018 cosmology (Planck Collaboration et al. 2020a,b, their Table 7) with $H_0 = 67.66\,\mathrm{km\,s^{-1}\,Mpc^{-1}}$, $\Omega_\mathrm{b} = 0.0489$, $\Omega_\mathrm{m} = 0.3111$, and $\Omega_\Lambda = 0.6889$.

2. *Euclid* observations and the *Planck* protocluster candidates sample

2.1. Euclid observations and data processing

Euclid observed the three deep fields, and the Q1 data release (Aussel et al. 2025) selects the passes corresponding to the depth of the wide survey. Processing is performed by the science ground segment (SGS) from images delivered by the VIS (Euclid Collaboration: Cropper et al. 2024; Euclid Collaboration: McCracken et al. 2025) and NISP instruments (Euclid Collaboration: Jahnke et al. 2024; Euclid Collaboration: Polenta et al. 2025). Here we use the photometric channels dubbed NIR. We make use of the multiwavelength photometric catalogue delivered by the "merged" processing function (Euclid Collaboration: Romelli et al. 2025), the MER processing function (PF), or MER in short, and the "photometric redshift" PF (Euclid Collaboration: Tucci et al. 2025), or PHZ in short. We use the *Euclid* VIS (see Appendix A) and NIR stacks tiles in bands I_E, Y_E, J_E, and

[1] *Planck* mission: Planck Collaboration et al. (2020a)
[2] https:rubinobservatory.org
[3] https:roman.gsfc.nasa.gov

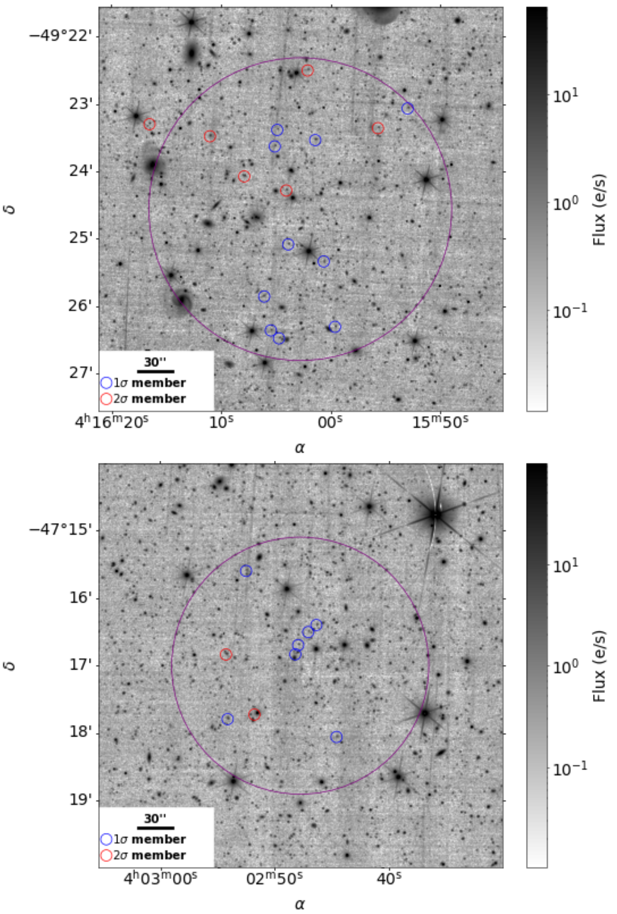

Fig. 1. *Euclid* NIR $H_{\rm E}$ images of the G257 protcluster detected by DETECTIFz at $z_{\rm ph} = 1.62^{+0.23}_{-0.26}$ (top) and the G254 protcluster detected by DETECTIFz at $z_{\rm ph} = 1.48^{+0.3}_{-0.12}$ (bottom). The cutouts cover $5' \times 5'$. The large purple circle represents the radius of the structure determined by DETECTIFz. Small blue circles correspond to galaxies belonging to the structure. Small red circles correspond to galaxies close to the structure, located at 2σ in photometric redshift.

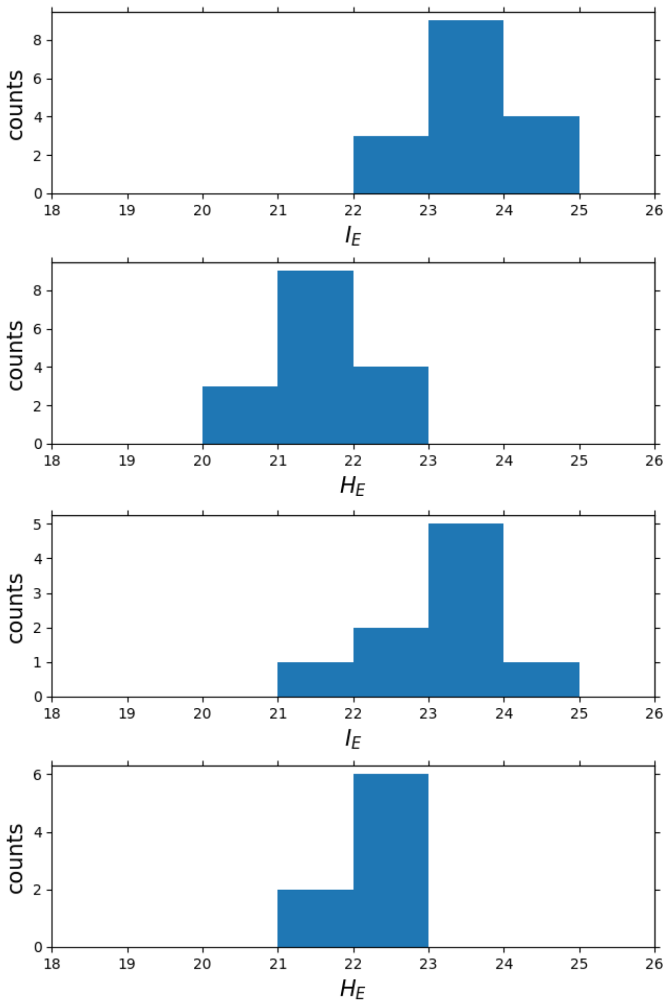

Fig. 2. Histogram of $I_{\rm E}$ (first and third lines) and $H_{\rm E}$ (second and fourth lines) magnitudes of the galaxies belonging to the G257 protocluster (top two plots) and G254 (bottom two plots).

$H_{\rm E}$ delivered by MER for visual inspection, together with the photometric redshift probability distribution function (PDF), the distribution of magnitudes and colours.

The MER photometric catalogue is merged with the PHZ photometric redshift catalogue and the resulting catalogue used as an input for the detection protocluster algorithms.

2.2. Protocluster sample used for biased detections: the *Planck* sample

In this study, we use the *Planck* catalogue of 2151 protocluster candidates (Planck Collaboration et al. 2016), the *Planck* catalogue of high-redshift sources over 28% of the sky. It was complemented by 228 deep *Herschel*/SPIRE[4] observations by Planck Collaboration et al. (2015b), but only 91 *Planck* sources ended-up in the final *Planck* catalogue. Approximately a hundred observations in the near-IR (NIR) were also performed with *Spitzer*[5] (Martinache et al. 2018). In addition, *Planck* protocluster candidates did happen to fall on the large *Herschel* surveys, where we use archival data from the *Herschel* Multi-tiered Extragalactic Survey (HerMES) (Oliver et al. 2012; Smith et al. 2012; Roseboom et al. 2010) in the EDF-F (Table 1).

The *Planck* protocluster candidates (Planck Collaboration et al. 2016) were selected by colour in the high frequency instrument (HFI) submm cleaned images, targeting $z \sim 2$ (groups of) IR galaxies, such as galaxies with significant star-formation activity. This sample is thus different from the Sunyaev-Zeldovich (SZ) sample (Planck Collaboration et al. 2015a). The cleaning procedure consisted in removing the cosmic microwave background (CMB) and Galactic cirrus emission. We refer the reader to Planck Collaboration et al. (2016) for details on the construction of the*Planck* catalogue of protocluster candidates. Soon after its publication, the purity of the protocluster catalogue was discussed. For example, Negrello et al. (2017), pointed out the possible presence of line-of-sight alignments of bright IR galaxies that potentially mimic, in the 4.′5 *Planck* beam, a single protocluster. Follow up observations of a few *Planck* fields confirmed that in several cases there are multiple structures aligned along the line of sight Flores-Cacho et al. (2016); Kneissl et al. (2019); Polletta et al. (2021, 2022); Hill et al. (2024).

Using IllustrisTNG simulations (Pillepich et al. 2018; Nelson et al. 2019), Gouin et al. (2022) reproduced the *Planck* selection and confirmed the contamination of star-forming sources along the line-of-sight but they also showed that more than 70%

[4] *Herschel*/SPIRE: Griffin et al. (2010)
[5] *Spitzer*: Werner et al. (2004); Soifer et al. (2008)

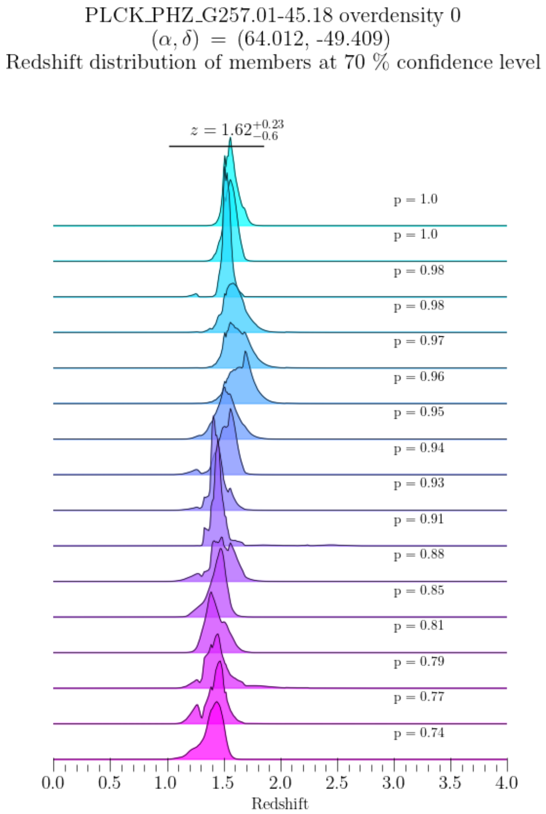

Fig. 3. Probability distribution functions of the photometric redshift of each of the 16 sources belonging to the G257 protocluster.

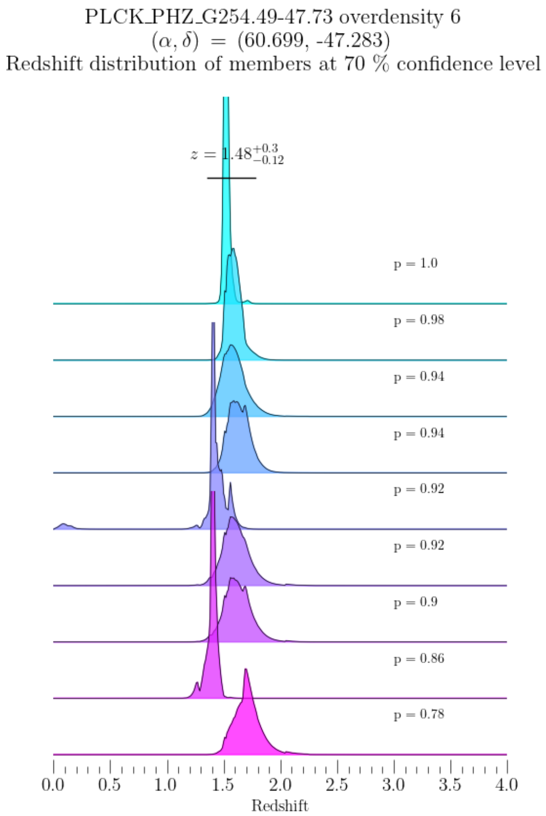

Fig. 4. Probability distribution functions of the photometric redshift of each of the nine sources belonging to the G254 protocluster.

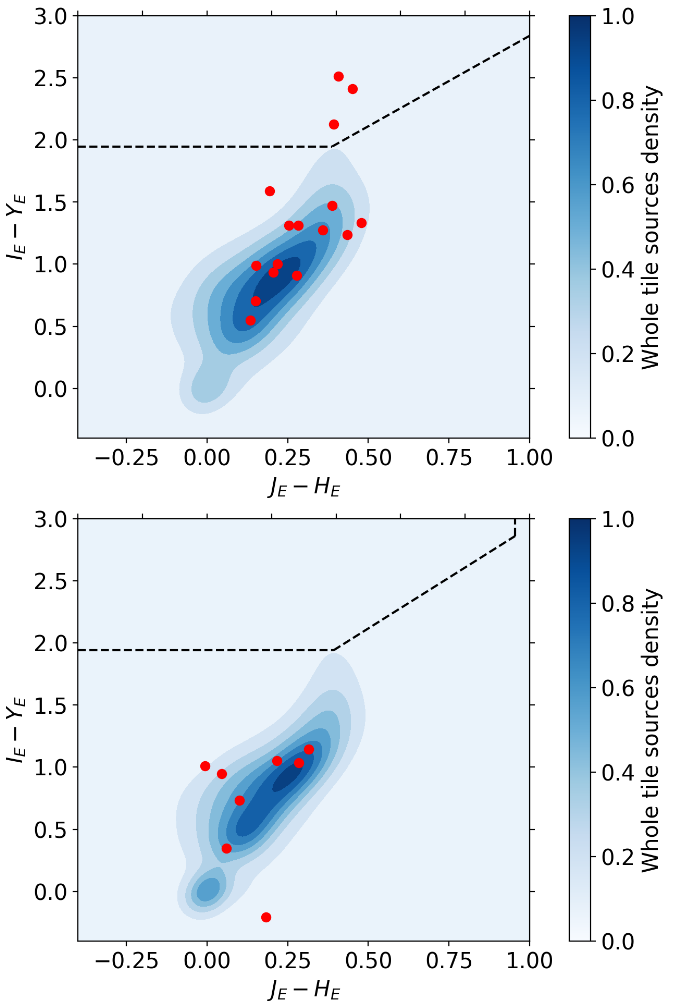

Fig. 5. $I_{\rm E} - Y_{\rm E}$ vs. $J_{\rm E} - H_{\rm E}$ pure *Euclid* colour-colour diagram of galaxies (red circles) belonging to the G257 protocluster (top) and G254 (bottom). The colours of all the sources of the tile (more than 100 000 sources) are shown in the blue background density. All sources (but three) of the G257 protocluster lie in the active galaxies region delimited by dotted black lines, as defined by Bisigello et al. (2020).

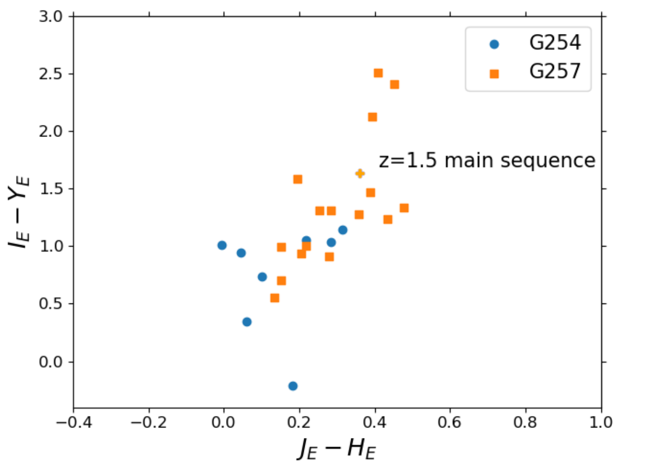

Fig. 6. $I_{\rm E} - Y_{\rm E}$ vs. $J_{\rm E} - H_{\rm E}$ pure *Euclid* colour-colour plot of the galaxies belonging to G257 (squares) and G254 (triangles). The main sequence point (circle) is computed from two models with respective initial masses of 10^{10} and $10^{11} M_{\odot}$ at $z = 8$, with a redshift corresponding to that of both overdensities.

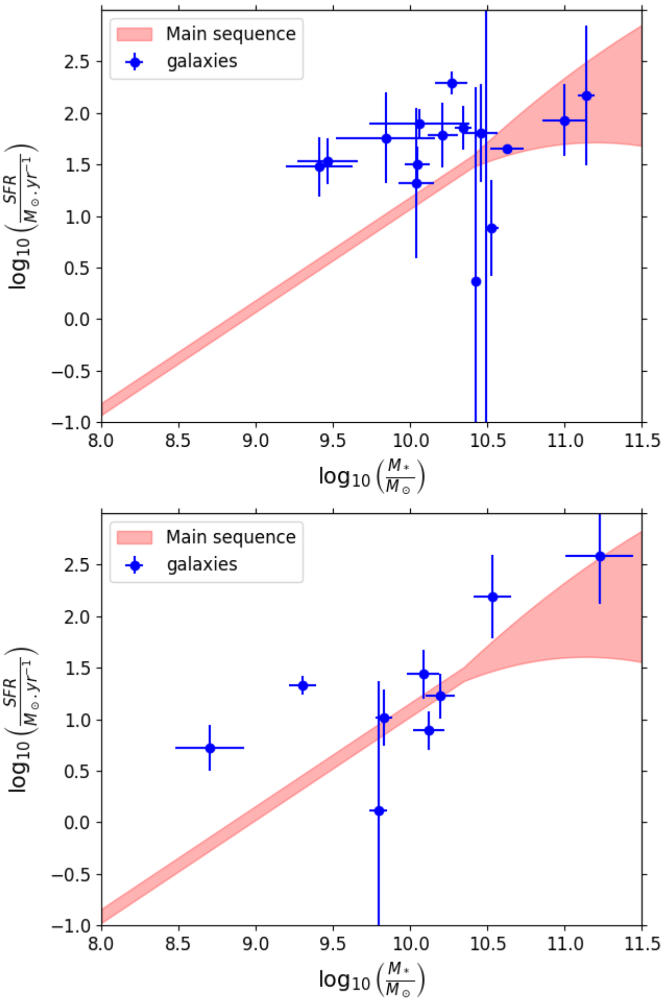

Fig. 7. Star-formation rate (SFR) vs. stellar mass ($M_\star$) of member galaxies of the G257 (top) and G254 (bottom) protoclusters. The model of Schreiber et al. (2015) for main sequence galaxies is overploted in red area, with model errors derived from the model parameters for a redshift $z = 1.62 \pm 0.25$ (top) and $z = 1.48 \pm 0.3$ (bottom).

of the *Planck* protocluster candidates should end-up as actual galaxy clusters by $z = 0$.

The *Planck* and complementary *Herschel* samples, both biased towards high star-formation rates (SFR), provided invaluable targets for multi-wavelength follow-up studies (e.g. Clements et al. 2014, 2016; Greenslade et al. 2018; Oteo et al. 2018; Cheng et al. 2019, 2020). Dedicated follow-up campaigns at optical, IR, and millimetric wavelengths (e.g. Flores-Cacho et al. 2016; MacKenzie et al. 2017; Kneissl et al. 2019; Polletta et al. 2021; Koyama et al. 2021; Lammers et al. 2022; Gatica et al. 2024) confirmed the redshift of a few protocluster candidates at the Cosmic Noon (z = 1.5–3) (see Polletta et al. 2022, for redshift information on most of the sources). More recently, Polletta et al. (2024) followed up the brightest *Herschel* source in one *Planck* protocluster candidate (i.e., PHz G191.24+62.04) with NOEMA and JWST/NIRCam, as part of the "JWST Prime Extragalactic Areas for Reionization and Lensing Science (PEARLS)" program (Windhorst et al. 2023). They found three counterparts, of which two at $z \sim 2.42$ and a third one at $z = 2.55$, and all three exhibit disk morphologies, extreme extinction, and widespread strong star-formation.

The *Planck* sample has also been used for spectral energy distribution statistical studies (see e.g., Kubo et al. 2019; Popescu et al. 2023; Gatica et al. 2024).

From this *Planck* sample, a total of 12 *Planck* protocluster candidates fall in the *Euclid* Q1 footprint, composed of three fields (Euclid Collaboration: Scaramella et al. 2022). Seven of *Planck* protoclusters candidate are situated in Euclid Deep Field South (EDF-S), five in Euclid Deep Field Fornax (EDF-F), and none in Euclid Deep Field North (EDF-N; see Table 1). Images from VIS instrument at the position of the *Planck* protocluster candidates are shown in Appendix A. For these 12 *Planck* protocluster candidates falling on the Q1 footprint, no spectroscopic information is available yet. As spectroscopic redshifts are lacking for most of the *Planck* protocluster candidates in general, this pilot study provides a first assessment of the *Planck-Euclid* synergy to probe star-forming galaxy protoclusters at Cosmic Noon.

3. Protocluster detection algorithms and selection

3.1. Selection for input

Each *Euclid* tile covers $30' \times 30'$ and contains on average 110 000 sources (Euclid Collaboration: Romelli et al. 2025). Uncertainties on photometry and astrometry come from the *Euclid* SGS MER (Euclid Collaboration: Romelli et al. 2025); Photometric redshifts (full probability distribution function, PDF), and derived physical parameters (mainly used here: stellar masses and SFRs) are obtained from PHZ (Euclid Collaboration: Tucci et al. 2025).

We select the *Euclid* sources in the MER and PHZ catalogues in the following way:

- $H_{\mathrm{E}} < 24$
- $\delta z_{\mathrm{ph}}/(1+z_{\mathrm{ph}}) < 0.10$, with z_{ph} being the median photometric redshift and δz_{ph} the uncertainty (taken at 68% of the PDF, the photo-z PDF).
- and sources not excluded by the masks avoiding the vicinity of bright stars or remaining artefacts **++TODO++ AS A CHECK XXXX.**

as an input for the protocluster search algorithms.

3.2. DETECTIFz

To identify the counterparts of the *Planck*-detected protocluster candidates, we apply the DETECTIFz (DElaunay TEssellation ClusTer IdentiFication with photo-z) algorithm (Sarron & Conselice 2021) on the 12 *Euclid* tiles containing a *Planck-Herschel* protocluster candidate. The DETECTIFz algorithm uses the Delaunay Tessellation Field Estimator (DTFE) to identify extended galaxy overdensities within redshift slices. This method is entirely empirical and model-independent, relying exclusively on galaxy sky coordinates and samples drawn from the photometric redshift probability distribution.

Beginning with a galaxy catalogue containing sky coordinates and photometric redshift probabilities, DETECTIFz constructs a 3D overdensity map. Overdensities are estimated in redshift slices spaced by 0.01 and with varying widths of $\pm 1\sigma_z(z)$, derived from the input galaxy catalogue. For each slice, DETECTIFz generates 100 Monte Carlo realisations of the overdensity map by sampling from the photometric redshift probability distribution and applying DTFE to each sample. The final density map is obtained by averaging over these realizations.

Within each slice, overdensities are identified as extended peaks in the density map. For each detection, the algorithm

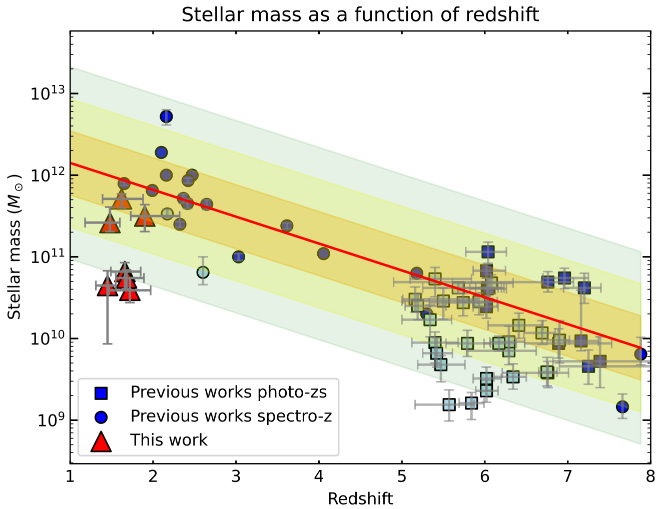

Fig. 8. Stellar mass (lower limits) as a function of redshift for the *Euclid* protoclusters (triangles) and from the literature: Casey (2016); Polletta et al. (2021); Laporte et al. (2022); Morishita et al. (2023, 2024); Sillassen et al. (2024); Gómez-Guijarro et al. (2019); Li et al. (2024); Shimakawa et al. (2024). A fit is performed on the data excluding *Euclid* (red line), with the scatter showed at 1σ (orange zone), 2σ (green zone), and 3σ (blue zone).

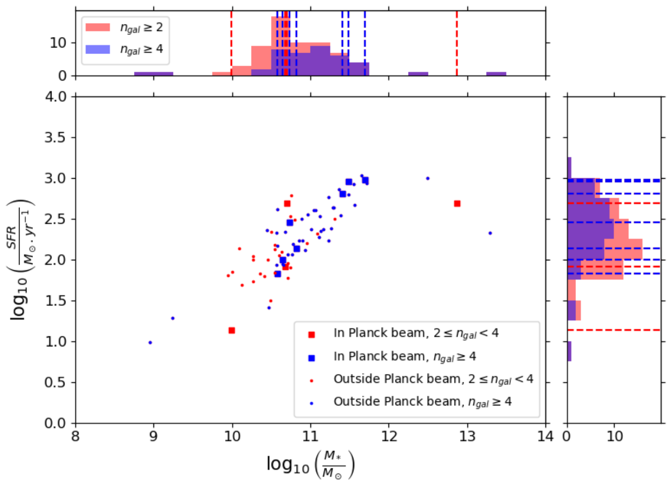

Fig. 9. Star formation rate as a function of stellar mass of the *Euclid* protoclusters. Dots represent overdensities with two or three galaxy members (red) or with four or more galaxy members (blue) outside the *Planck* beams. Filled squares are the overdensities associated with a *Planck* protocluster candidate, with two or three galaxy members (red square), or with four or more galaxies (blue square). Histograms for stellar masses (top) and SFR (right) are plotted using only detections outside of the Planck beams. Dashed lines represent the values corresponding to the 11 detections inside the Planck beams.

records a bounding box ($\mathrm{RA_{min}}$, $\mathrm{RA_{max}}$, $\mathrm{Dec_{min}}$, $\mathrm{Dec_{max}}$) that encloses regions with pixel values above the $(\mathrm{S/N})_{\mathrm{min}}$ threshold. To eliminate multiple detections of the same protocluster across adjacent slices or substructures, the algorithm merges peaks that are contiguous along the line of sight (i.e., in the redshift direction) and have either overlapping bounding boxes or peak separations of less than 2 comoving Mpc. These merged regions constitute the final galaxy protocluster candidates.

This selected sample (Sect. 3.1) is used as an input for DETECTIFz, to which we provide: celestial coordinates, and the full photometric redshift PDF. We force DETECTIFz to search for the redshift range 1.35–3.5, and to select only structures above a signal-to-noise ratio (S/N) of 1.5σ. DETECTIFz produces a list of overdensities and includes S/N, measurements of overdensity and radius (Sarron & Conselice 2021). In DETECTIFz, S/N is computed for each detection in each slice, within a disk of fixed radius of 500 comoving kpc[6] around the peak. For each slice, we calculate the mean (μ_δ) and standard deviation (σ_δ) of the entire density map, after applying a 3σ-clipping to remove outliers. The mean overdensity signal in the region around the peak is then compared to these global values to form the S/N:

$$\mathrm{S/N} = \frac{\langle \log(1+\delta) \rangle_{R_{500\,\mathrm{ckpc}}} - \mu_\delta}{\sigma_\delta} \quad (1)$$

We find a total of 259 'raw' overdensities with SNR> 1.5 on the 12 *Euclid* tiles. Among those, some need to be discarded of our analysis because of a too low SNR, or contamination by bright stars, foreground galaxies and photometric artifacts. After removing these, we are left with 81 viable detections.

[6] This is equivalent to a radius of ∼0′.4 at $2.5 < z < 3.5$, and ∼0′.5–0′.6 at $1.35 < z < 2$. This radius is >10 times smaller than the *Planck* beam (FWHM≃4′.7), and similar to the *Herschel* beam (FWHM∼24″ at 350μm).

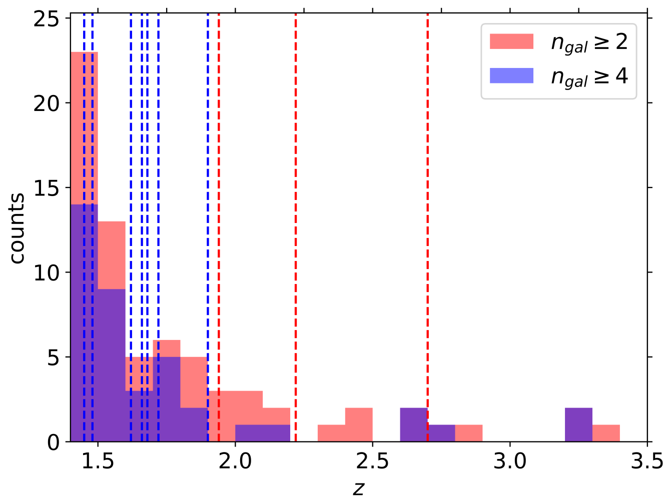

Fig. 10. Photometric distributions of the *Euclid* overdensities . Red: overdensities with two or more galaxy members; Blue: with four or more galaxy members outside the *Planck* beams. Vertical dashed lines represent the values corresponding to the 11 detections inside the Planck beams : with two or three galaxy members (red), or with four or more galaxies (blue).

3.3. Post-selection after DETECTIFz

After running DETECTIFz, we post-select the protoclusters satisfying simultaneously these conditions:

- (a) contain galaxies with more than 68% probability to be a member, and no sign of artifact due to a foreground star;
- (b) protoclusters having at least two (criterion b1) galaxy members, or four members (criterion b2);
- (c) falling within a *Planck* beam.

We have at this stage: 81 protoclusters meeting criteria a+b1; 34 meeting criterion a+b2; And finally 11 meeting criteria a+b1+c and 7 meeting criteria a+b2+c.

The two most significant detections at the locations of *Planck* protocluster candidates are reported in Table 2 with S/N > 4.7. Five relatively secure detections, with S/N > 2.08 are reported in Table 3. We also show a few tentative detections (S/N > 1.9) but containing only two or three galaxies members, in Table C.1.

From now on, we will call "protoclusters" the structures detected by DETECTIFz in the *Euclid* data and associated with a *Planck* protocluster candidate (see Sect. 5).

3.4. Euclid protoclusters vs. Euclid-Planck

Here, we asses whether the overdensities falling within the beam of a *Planck* protocluster candidate are random or bona-fide counterparts. The DETECTIFz search uncovered 81 overdensities with S/N>1.5 over the 50 deg^2 of the Q1 *Euclid* field. There are 12 *Planck* protocluster candidates in the field, covering in total an area of about 0.26 deg^2 (assuming circular regions of 5′ radius). We thus expect to find only 0.42 overdensities randomly associated with the *Planck* protoclusters. Finding 11 *Euclid* overdensities within the *Planck* fields implies that the *Euclid-Planck* associations are highly significant and that they are bona-fide counterparts.

To investigate whether the *Euclid-Planck* overdensities are characterized by distinctive properties with respect to the rest of the *Euclid* overdensities, we compare their total SFRs and stellar masses in Fig. 9 and distinguish those with more or less than three members. The *Euclid-Planck* overdensities sub-set covers a similar range of SFRs, stellar masses and richness. We also check the photometric distributions (Fig. 10). It is thus not clear why some of these overdensities are also detected by *Planck* and others are not. We will investigate in the future whether the *Planck* fields host additional overdensities at higher redshifts.

3.5. PPM and MC-DTFE-LoG

We consolidate the detections of protocluster counterparts using two other independent algorithms.

We use the Poisson probability method (PPM) The PPM searches for high-z megaparsec-scale overdensities of galaxies around a given target. It is based on a theory defined on the ensemble of the photometric redshift realizations of the galaxies in the field. Through the use of a solid positional prior and an accurate photometric redshift sampling, the PPM partially overcomes the limitations deriving from low number-count statistics and shot-noise fluctuations, which are particularly relevant in the high-z universe such as in the case of protoclusters. More specifically, the PPM method uses photometric redshifts of galaxies to search for overdensities around each target along the line of sight. In this work, we used the projected space coordinates of Planck-Herschel overdensities, as well as DETECTIFz and DFTE projected space coordinates, separately. To search for associated overdensities, the PPM adopts an accurate sampling of the photometric redshift information to the detriment of a less sophisticated tessellation of the projected space, which is performed in terms of concentric annuli centered around each target. We refer to our previous studies for a detailed description of the method (Castignani et al. 2014a,b), its wavelet based extension (wPPM Castignani et al. 2019), and the applications (Castignani et al. 2014b, 2019; Calvi et al. 2023)). PPM is run at the sky locations of the DETECTIFz positions as input (as well as the *Planck* protocluster coordinates for checks).

We also use a newly developed detection code for galaxy protoclusters at z > 1.5, fine-tunned for *Euclid*-like WIDE survey (Ramos Chernenko et al. 2024). The detection code is based on the Monte-Carlo Delaunay Tesselation Field Estimator (Schaap & van de Weygaert 2000; Schaap 2007), combined with the Laplacian of Gaussian (Sotak & Boyer 1989; Lindeberg 1992) filter (MC-DTFE-LoG, hereafter). In concept, MC-DTFE-LoG is similar to DETECTIFz algorithm, but enhanced with a multiscale 3D source detection filter. The 3D Gaussian filters were specifically calibration using *Euclid*-like protoclusters properties from GAEA and MAMBO simulations Euclid Collaboration et al. (2025). The proposed approach is now being tested and validated for a systematic detection of galaxy protoclusters in *Euclid*-like WIDE survey using the Q1 data (Ramos Chernenko et al. 2025).

Finally, both algorithms found the two significant structures at the same sky positions and photometric redshifts than those outputted by DETECTIFz. Table 4 reports the detections and S/N, similar to DETECTIFz, discussed in Sect. 5.1.

4. *Euclid* protoclusters associated with the 12 *Planck* protocluster candidates

4.1. The two most significant protoclusters: G257 and G254

The two most significant *Euclid* protocluster detections, counterparts of *Planck* protocluster candidates (reported in Table 2) are G257.01-45.18_0 (G257 thereafter; S/N=6.75) with 16 members at photometric redshift $z_{\rm ph} = 1.62^{+0.23}_{-0.26}$ and G254.49-47.73_6 (G254; S/N=4.75) with 9 members at $z_{\rm ph} = 1.48^{+0.3}_{-0.12}$. Figure 1 shows the NIR $H_{\rm E}$ images of G257 and G254 and the associated galaxy members.

Figure 2 shows the histogram of the $I_{\rm E}$ and $H_{\rm E}$ magnitudes of the protocluster members. The fact that we select galaxies with $H_{\rm E} < 24$ for the protocluster search does not prevent fainter galaxies to belong to the protocluster (same sky positions and photometric redshifts) in the end in principle; however, in this pilot study we barely encounter this case. Due to the preselection in photometric redshift and magnitude (see Section 3), it is possible that some members galaxies of the overdensities are not detected. Thus, all the parameters such as the total stellar mass $M_\star$ and SFR should be considered as lower limits, although the contributions of the undetected sources are not expected to be significant.

4.2. Photometric redshifts and colours

The PDF of the photometric redshifts of the G257 and G254 protocluster members is shown in Fig. 3. Ensuring a homogeneous distribution of those PDFs is one of the main criterion to retain a protocluster in our final list. Figures in Appendices B show the photometric redshift PDF of each protocluster member.

The pure *Euclid* colour-colour diagrams, $I_{\rm E} - Y_{\rm E}$ vs. $J_{\rm E} - H_{\rm E}$, are shown in Figs 5, 6, following Bisigello et al. (2020). The vast majority of galaxies is star-forming galaxies. In Fig. 5, we show the G257 protocluster galaxy members (red points) together with the ∼100 000 sources in the tile (blue background density). In order to help the interpretation of colours, we show in Fig. 6 the colours of galaxy members of the protoclusters G257 and G254, together with the expected colours of a $z = 1.5$ main sequence galaxy from the GALEV models (Kotulla et al. 2009).

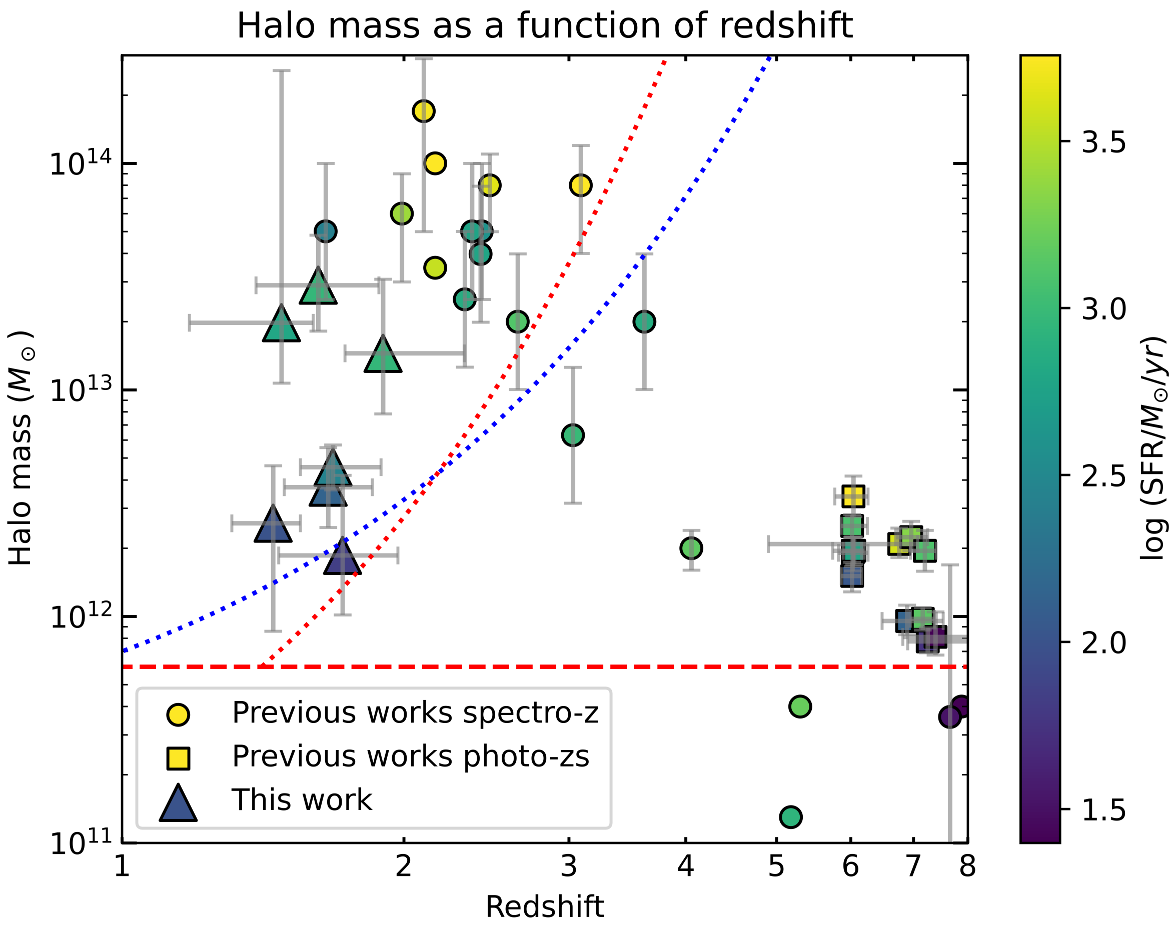

Fig. 11. Protocluster halo mass (M_h) vs. redshift z (notice the log-log scale), colour-coded by star-formation rate (SFR, right colour bar). *Euclid* protoclusters lower limits: triangles, using method b [S22] (Shuntov et al. (2022), see Sect. 4.4 for details). Circles: protoclusters from the literature: Casey (2016); Polletta et al. (2021); Laporte et al. (2022); Morishita et al. (2023, 2024); Sillassen et al. (2024); Shimakawa et al. (2024). The lines illustrate the different predicted gas cooling regimes: dotted lines come from Dekel & Birnboim (2006) (red dot) and Daddi et al. (2022) (blue dot) and separate loci of cold gas in hot medium (top right) and hot gas (top left); Halo masses below the horizontal dash line M_shock, coming from Dekel & Birnboim (2006), are predicted to contain only cold flows with no shock heating within haloes. The *Planck* protoclusters first seen by *Euclid* start to fill the previously poorly-populated transition zone near ($z \sim 1.5$, $M_\mathrm{h} \sim 10^{12}$–$3.10^{13}$ $M_\odot$).

4.3. Physical parameters: stellar masses, star-formation rates

We use the physical parameters derived by the photometric redshift estimation procedure. Figure 7 shows the SFR-$M_\star$ relation for the galaxy members of G257 and G254, together with the main sequence model of Schreiber et al. (2015). This relation assumes that SFR and stellar mass $M_\star$ are linearly correlated (SFR $\propto M_\star$) below a mass and redshift threshold, above which the SFR decreases with galaxies gradually quenched.

We observe that in G257, most galaxies lie above the main sequence, a clear sign of starburst activity, yielding a total SFR, as measured by *Euclid*, of $\log_{10}(\mathrm{SFR}/M_\odot\,\mathrm{yr}^{-1}) \sim 2.97$ (Table 2). The source G254, at lower redshift, shows a smaller fraction of starburst galaxies and less members than G257, but a similarly high total SFR, $\log_{10}(\mathrm{SFR}/M_\odot\,\mathrm{yr}^{-1}) \sim 2.80$.

The five other protoclusters (Table 3) also exhibit relatively high SFR, $\log_{10}(\mathrm{SFR}/M_\odot\,\mathrm{yr}^{-1}) \sim 1.80$–$2.96$ (Table 3) and most of the member galaxies lie on the main sequence (except for G254_17 showing strong signs of starburst activity).

We compute the total stellar masses of each protocluster (Table 2 and 3) by summing-up the stellar masses of individual galaxies. This can be taken as a lower limit of the protocluster stellar mass. Indeed, our protocluster members are choosen to have at least 68% probability to be a member.

In Figure 8 we report the protocluster stellar masses vs. redshift. The three protoclusters having the largest stellar masses are expectedly the higher S/N detection with DETECTIFz. Their stellar masses are lower, but in line with the literature, within 2σ. The four least massive *Euclid* protoclusters, are however less massive than the literature at more than 3σ, likely because we identify only a few member galaxies (between 4 an 7), thus the lower limit appears low. Gouin et al. (2022) showed on simulations that a structure with more tha 3 star-forming galaxies and selected as a *Planck* protocluster candidate could still have 70% probability to become a cluster at $z = 0$.

Finally, we report in Tables 2 and 3 the observed radius of the protoclusters. The values, of the order of 2′, are about a factor of two smaller than the predictions of Euclid Collaboration et al.

(2025) for protoclusters of mass larger that $10^{14}\,M_{\odot}$ at $z = 1.5$ or 2.

4.4. Halo masses

There are a few methods to estimate the halo mass $M_{\rm h}$ of the protoclusters (Long et al. 2020; Champagne et al. 2021; Daddi et al. 2022; Laporte et al. 2022; Sillassen et al. 2024) from the measurements of stellar masses of their member galaxies. Most of them are based on "calibrated" relations between stellar masses and halo mass (Behroozi et al. 2013; van der Burg et al. 2014; Behroozi et al. 2019; Legrand et al. 2019; Girelli et al. 2020; Shuntov et al. 2022).

In this study, we use two methods. The first (method a) uses the universal cosmological baryonic fraction $\Omega_{\rm m}/\Omega_{\rm b} - 1 = 5.35$ (Planck Collaboration et al. 2020a,b) to estimate the cold dark matter mass of the halo. The second (method b) relies on the relationship between the galaxy stellar mass and the halo mass, tabulated from Behroozi et al. (2013)[B13], Legrand et al. (2019)[L19], and Shuntov et al. (2022). The halo masses of the detected protoclusters are thus estimated from their total stellar masses based on the stellar-to-halo mass relation from [B13], [L19] and [S22]. The latter method assumes virialisation of the cluster core, while the former does not account for the missing baryon problem (Nicastro et al. 2018) and can be seen as a lower limit.

Uncertainties are computed by propagating the errors on stellar masses from the *Euclid* PHZ physical parameters catalogues (Euclid Collaboration: Tucci et al. 2025) and also using each model parameter uncertainty as provided by [B13], [L19] and [S22]. The estimated halo masses are reported in Table 5 for both methods and they are shown in Fig. 11 for method b [S22]. The three estimates using the method b are consistent within at most 0.5 dex differences, and the halo masses derived using the prescriptions from Legrand et al. (2019) and Shuntov et al. (2022) usually agree to better than 0.1 dex (typically < 0.04 dex).

The seven *Planck* and *Euclid* protoclusters occupy a "sweet spot" in the $[\log_{10}(M_{\rm h}), z]$ plane (Fig. 11) around (12.0–13.3, 1.5–2): in this locus, haloes of forming galaxy clusters are expected to experience a transition between cold flows with no shock heating throughout the halo to shock heating in the halo (Dekel & Birnboim 2006; Daddi et al. 2022). *Euclid* and *Planck* protoclusters may allow a better probe of this still enigmatic regime change.

We can notice that our three best detections, among which G257 and G254, are more massive than the four other protoclusters (lower limits) of this pilot study.

5. Discussion

5.1. Line-of-sight effects ?

While PPM and MC-DTFE-LoG find similar sources as DETECTIFz (Table 4) and are in agreement, other overdensities are detected. The PPM algorithm finds also, at the location of the *Euclid* DETECTIFz source G254, three background overdensities with a S/N of 2.2 each, at redshifts $z = 1.9$, 2.3 and 2.8. For the source G257, background sources are found at redshifts $z = 2.8$ and 3.9 with a S/N of 2.9 each. For the source G221, PPM finds overdensities bt decreasing S.N from 4.9 down to 2.4 at redshifts $z = 3.6$ and 4.6. For the source G222, a few overdensities with S/N<2.6 at redshifts $z = 2.5$, 3.0 and above. And for the source G224, background overdensities are detected with S/N=2.4 at $z = 2.1$, 3.6.

The multiplicity of background overdensities detected with similar S/N raises the question of actual matching of the *Euclid* overdensities with the *Planck* protocluster candidate, expected at $z > 2$. While this issue might require the DR1 data to be investigated, one possibility is that our procedure preferentially detects foreground overdensities.

5.2. Are they protoclusters? Are they Planck protoclusters?

The three most massive *Euclid* protoclusters (Fig. 11) show characteristics comparable to protoclusters from the literature. Four other protoclusters show lower masses, by about an order of magnitude, which raises the question of their actual nature.

Many galaxies in the *Euclid* protoclusters are experiencing a "star formation event", or a starburst. This could be another indication that *Euclid* actually detects the counterparts of the *Planck* protocluster candidates.

But there is little clear evidence that all these structures are starbursting, despite the *Planck* high SFR. Previous works on the *Planck* protocluster candidates (Polletta et al. 2021, 2022; Kneissl et al. 2019; Hill et al. 2024)) have shown that the majority of the protocluster members are on the main sequence. This seems to be the case also in other protoclusters like the Spiderweb (Pérez-Martínez et al. 2024a), although not in all, like USS 1558-003 (Pérez-Martínez et al. 2024b) and some of the member galaxies here.

To further reinforce this analysis, we can use and compare both *Euclid* and *Planck*-derived SFR. Because of the redshift-dust temperature degeneracy at submm wavelengths, Planck Collaboration et al. (2016) provided estimates of the submm photometric redshift, far-IR (FIR) luminosities, and SFRs of the protocluster candidates corresponding to different dust temperatures. Here, as a first approach, we look at the *Planck* submm photometric redshifts, and take the closest to the *Euclid* $z_{\rm ph}$ which selects a dust temperature. In most cases, the temperature of the dust component that yields a good match between *Planck* and *Euclid* photometric redshifts is $T = 25$K. The only exceptions are sources G224 and G221 for which the best match is obtained by assuming $T = 30$K, and $T = 35$K, respectively. Without discussing here the relevance of this temperature, selecting this dust temperature allows us to estimate the FIR luminosity and the SFR, given in Tables 2 and 3. *Planck*-derived SFR are usually around 1.8 dex higher than the *Euclid*-derived SFR. This is not surprising, given that *Planck* measurements encompass a larger physical scale (Negrello et al. 2017; Gouin et al. 2022) in terms of angular scale but also in line-of-sight contributions.

Five out of the seven protoclusters have also full or partial *Herschel* coverage. Data come from Oliver et al. (2012) in the EDF-F, and from Planck Collaboration et al. (2015b) in the EDF-S (Table 1). The protoclusters in G254.49-47.73 and G222.75-55.98 have partial coverage because they are close to the edge of the *Herschel* images. For each protocluster we computed the total SFR considering only the *Herschel* sources within the overdensity radius (see Table 3), and with $> 3\sigma$ detections in all three SPIRE bands. We fitted the submm data of each selected *Herschel* source with a modified greybody using the `cmcirsed` package (Casey 2012), and assuming the protocluster redshift and a dust emissivity-index β equal to 1.8 (Cortese et al. 2014; Pokhrel et al. 2016). To avoid contamination from *Herschel* sources at a redshift incompatible with that of the protoclusters, we included in the total SFR estimate only the sources for which the fit yielded a dust temperature >15 K and <50 K. The SFR of each source was derived from the total FIR luminosity as SFR = 1.48×10^{-10} L(FIR) (Kennicutt & Evans 2012). In Table

Table 2. Highly significant *Euclid* protoclusters detected with DETECTIFz at the location of *Planck* & *Herschel* protocluster candidates. Column decsription: *Planck* name; DETECTIFz photometric redshift, based on *Euclid* photometric redshifts; Number of galaxies in the protocluster; DETECTIFz overdensity; Stellar mass of the protocluster (the sum of stellar masses of all galaxies, coming from *Euclid* PHZ); SFR of the protocluster (the sum of the SFR of all galaxies, coming from *Euclid* PHZ); Radius of the protocluster, as estimated by DETECTIFz; *Planck* SFR.

Planck field name	$z_{\rm ph}$	N Gal	S/N	Overdensity $\log_{10}[1+\delta]$	$M_\star$ tot $\log_{10}[M_\odot]$	SFR tot $\log_{10}[M_\odot\,{\rm yr}^{-1}]$	Radius arcmin	SFR *Planck* $\log_{10}[M_\odot\,{\rm yr}^{-1}]$
G254.49-47.73	$1.48^{+0.3}_{-0.12}$	9	4.75	0.32	$11.42^{+0.19}_{-0.11}$	$2.80^{+0.41}_{-0.34}$	$1'.90$	4.15 ± 0.2
G257.01-45.18	$1.62^{+0.23}_{-0.26}$	16	6.75	0.62	$11.71^{+0.06}_{-0.11}$	$2.97^{+0.27}_{-0.21}$	$2'.24$	4.03 ± 0.15

Table 3. Selected *Euclid* protoclusters detected with DETECTIFz at the location of *Planck* & *Herschel* protocluster candidates. Column are the same as Table 2.

Planck field name	$z_{\rm ph}$	N Gal	S/N	Overdensity $\log_{10}[1+\delta]$	$M_\star$ tot $\log_{10}[M_\odot]$	SFR *Euclid* $\log_{10}[M_\odot\,{\rm yr}^{-1}]$	Radius arcmin	SFR *Planck* $\log_{10}[M_\odot\,{\rm yr}^{-1}]$	N	SFR *Herschel* $\log_{10}[M_\odot\,{\rm yr}^{-1}]$
G221.09-54.59	$1.90^{+0.17}_{-0.42}$	12	2.8	0.18	$11.50^{+0.14}_{-0.19}$	$2.96^{+0.40}_{-0.50}$	$4'.12$	4.64 ± 0.15	38	$4.16^{+0.03}_{-0.02}$
G222.75-55.98	$1.45^{+0.14}_{-0.10}$	5	2.06	0.31	$10.65^{+0.18}_{-0.71}$	$2.0^{+0.40}_{-0.48}$	$1'.32$	4.24 ± 0.15	3	$2.96^{+0.08}_{-0.07}$
G224.36-53.19	$1.66^{+0.17}_{-0.19}$	4	2.76	0.37	$10.82^{+0.11}_{-0.22}$	$2.14^{+0.18}_{-0.16}$	$2'.24$	4.46 ± 0.15	8	$3.35^{+0.07}_{-0.05}$
G254.49-47.73	$1.72^{+0.25}_{-0.25}$	4	2.65	0.23	$10.59^{+0.15}_{-0.15}$	$1.83^{+0.31}_{-0.26}$	$2'.21$	4.15 ± 0.2	5	$3.43^{+0.15}_{-0.11}$
G254.49-47.73	$1.68^{+0.13}_{-0.21}$	7	2.27	0.21	$10.74^{+0.10}_{-0.13}$	$2.45^{+0.23}_{-0.26}$	$2'.49$	4.15 ± 0.2	1	$2.62^{+0.28}_{-0.28}$

Table 4. PPM and MC-DTFE-LoG independant detections at the locations of the *Euclid* counterparts of the *Planck* protocluster candidates. Columns: field name; PPM redshift of the overdensity (based on photometric redshifts); PPM S/N of detection. MC-DTFE-LoG redshift of the overdensity (based on photometric redshifts); MC-DTFE-LoG S/N of detection.

Planck field name	$z_{\rm ph}$ [PPM]	S/N [PPM]	$z_{\rm ph}$ [MC-DTFE-LoG]	S/N [MC-DTFE-LoG]
G254.49-47.73	1.55 ± 0.09	3.9	1.84 ± 0.24	5.0
G257.01-45.18	1.41 ± 0.09	7.7	1.36 ± 0.24	1.7
G221.09-54.59	1.98 ± 0.09	2.1	1.88 ± 0.24	5.9
G222.75-55.98	1.31 ± 0.09	8.0	1.36 ± 0.24	2.6
G224.36-53.19	1.71 ± 0.09	2.2	1.60 ± 0.24	3.2
G254.49-47.73	1.82 ± 0.09	2.4	1.84 ± 0.24	2.1

3, we report the total SFR and the number of *Herschel* sources included in the computation. The number of selected *Herschel* sources range from one to 38 and the *Herschel*-based total SFRs are about 1.5–40 times larger than those derived from the *Euclid* PHZ. This wide disparity might be explained by incompleteness in the *Euclid* selected members and by contamination of *Herschel* sources that are not protocluster members.

The presence of submm bright structures at higher redshifts than those found by DETECTIFz will be explored further, for instance with the MC-DTFE-LoG algorithm that was specifically created to detect galaxy protoclusters at $z > 1.5$ and PPM at the detected locations.

5.3. Their evolutionary state: are they in the "dying protocluster" phase (or "protocluster swan song") ?

The G257 and G254 protoclusters (and the five other *Planck-Euclid* protoclusters of this pilot study) are characterized by high SFRs, and are located towards the end of Cosmic Noon, at redshifts $z_{\rm ph}$ = 1.45–1.90. In this redshift range, several mature galaxy clusters are already detected (e.g., Willis et al. 2020; Stanford et al. 2012; Gobat et al. 2013; Andreon et al. 2014; Strazzullo et al. 2023). The star forming nature of the member galaxies and the high total SFRs suggest that these protoclusters might be in an earlier evolutionary stage than the more mature coeval galaxy clusters. However, this star formation activity is not expected to be fueled by cold gas accretion as the gas is expected to be shock heated, as illustrated in Fig. 11. Thus, what makes these protoclusters special at these relatively low redshifts ? Will some not become galaxy clusters ? In which evolutionary state are we observing these protoclusters ? How is the observed star formation activity sustained ? While it is difficult to accurately answer these questions given the available data, we may provide a hypothesis.

Using molecular gas observations, Polletta et al. (2022) (their Sect. 4.9) find that other *Planck* protoclusters located at $z > 2$ exhibit gas depletion times of the order of $\langle\tau_{\rm dep}\rangle = 0.47 \pm 0.07$ Gyr, and are thus expected to exhaust their cold gas at around $z \sim 1.1$–1.6. Might we actually be observing these "dying protoclusters", and looking at the "protocluster swan song", i.e. their last unsustainable star-formation event or star formation event before a complete exhaustion of gas for star formation? The end of this dying protocluster phase may mark the maturing phase and the actual "birth" of a galaxy cluster. Molecular gas observations are also needed to address this question.

Table 5. Halo masses $M_{\rm h}$ for selected *Euclid* protoclusters detected with DETECTIFz at the location of *Planck* & *Herschel* protocluster candidates, obtained from the stellar masses with method a) and b) (Sect. 4.4). Method a uses the $\Omega_{\rm b}$ vs. $\Omega_{\rm m}$ ratio and can be viewed as a lower limit (column $M_{\rm h}$ (a)). Method b uses the stellar to halo mass relations from Behroozi et al. (2013) in column $M_{\rm h}$ (b [B13]), Legrand et al. (2019) in column $M_{\rm h}$ (b [L19]) and Shuntov et al. (2022) in column $M_{\rm h}$ (b [S22]). The first one is applied to the most massive galaxy stellar mass of the protocluster (column $M_{\star\rm central}$) whereas the second and third ones take dark matter haloes of each member galaxy into account. Name and ID refers to previous Tables 2 & 3.

Planck field name	ID	$M_{\star\rm central}$ $\log_{10}[M_\odot]$	$M_{\rm h}$ (a) $\log_{10}[M_\odot]$	$M_{\rm h}$ (b [B13]) $\log_{10}[M_\odot]$	$M_{\rm h}$ (b [L19]) $\log_{10}[M_\odot]$	$M_{\rm h}$ (b [S22]) $\log_{10}[M_\odot]$
G254.49-47.73	6	$11.22^{+0.22}_{-0.12}$	$12.22^{+0.23}_{-0.13}$	$12.85^{+0.34}_{-0.20}$	$13.29^{+1.32}_{-0.3}$	$13.3^{+1.11}_{-0.27}$
G257.01-45.18	0	$11.14^{+0.05}_{-0.05}$	$12.51^{+0.07}_{-0.12}$	$12.79^{+0.15}_{-0.14}$	$13.44^{+0.16}_{-0.15}$	$13.46^{+0.22}_{-0.2}$
G221.09-54.59	11	$10.83^{+0.18}_{-0.62}$	$12.23^{+0.20}_{-0.64}$	$12.59^{+0.19}_{-0.42}$	$13.16^{+0.19}_{-0.19}$	$13.16^{+0.33}_{-0.27}$
G222.75-55.98	16	$10.38^{+0.08}_{-3.8}$	$11.45^{+0.10}_{-3.8}$	$12.07^{+0.14}_{-0.96}$	$12.32^{+0.24}_{-0.44}$	$12.41^{+0.25}_{-0.47}$
G224.36-53.19	7	$10.32^{+0.11}_{-0.05}$	$11.62^{+0.13}_{-0.07}$	$12.33^{+0.11}_{-0.13}$	$12.56^{+0.11}_{-0.15}$	$12.57^{+0.17}_{-0.18}$
G254.49-47.73	14	$10.57^{+0.12}_{-0.13}$	$11.39^{+0.14}_{-0.15}$	$12.46^{+0.12}_{-0.18}$	$12.26^{+0.24}_{-0.18}$	$12.27^{+0.35}_{-0.26}$
G254.49-47.73	17	$10.11^{+0.04}_{-0.08}$	$11.47^{+0.06}_{-0.10}$	$12.23^{+0.07}_{-0.14}$	$12.62^{+0.07}_{-0.07}$	$12.66^{+0.1}_{-0.1}$

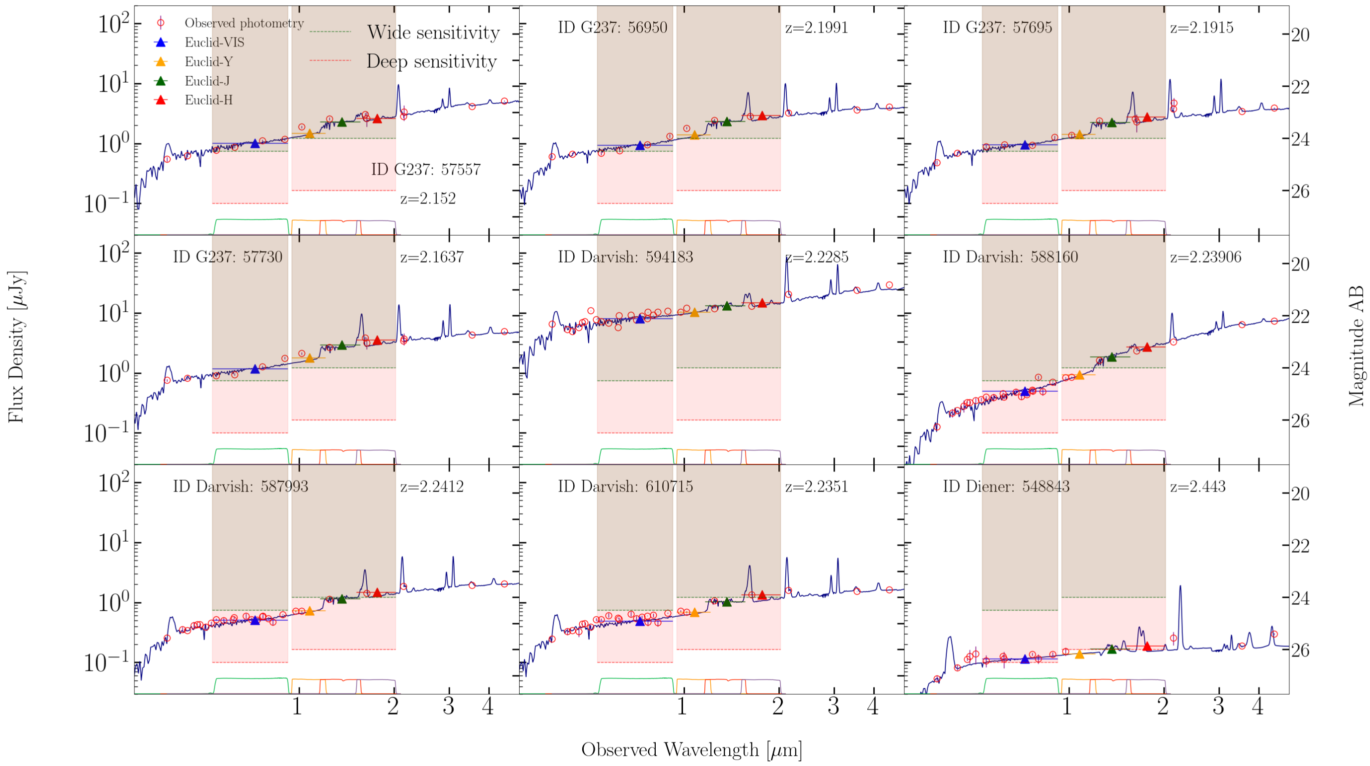

Fig. 12. Nine galaxies SED of spectroscopically confirmed protoclusters from Polletta et al. (2021), Diener et al. (2015) and Darvish et al. (2020), and their fit using Prospector (Johnson et al. 2021). Circles: photometric points. Coloured triangles: interpolated flux densities in the *Euclid* protometric bands. Green dashes: detection limit for the Euclid Wide Survey. Red dashes: detection limit for the Euclid Deep Survey. The *Euclid* bandpasses are represented in the bottom of each panel. The detectability zones (marron for Wide, red for Deep) illustrate the areas where galaxies will be detected by *Euclid*.

6. Prospects for future detections of galaxy protoclusters in *Euclid* Wide and Deep surveys: empirical approach

Looking ahead, beyond the first detections of protoclusters in this pilot project, we can ask ourselves what will be the properties (mainly the redshift distribution) of the protoclusters that will be detected by *Euclid* in the future. Simulations by Euclid Collaboration et al. (2025) provide forecasts on abundance, and sky-filling as a function of redshift, among other observables. They show that *Euclid* should detect around eight galaxy protoclusters per square degree at $z = 1.5-2$ with masses greater than $10^{14}\,M_\odot$.

Another, empirical, way to predict the detectability of galaxy protoclusters in the *Euclid* wide and deep surveys is to use existing protoclusters. We use individual galaxies belonging to spectroscopically confirmed protoclusters around $z \sim 2$ by Diener et al. (2015); Wang et al. (2016); Darvish et al. (2020); Polletta et al. (2021). This redshift range is rather similar to the photometric redshift of our detections. We fit the SED of the individual galaxies with `Prospector` (Johnson et al. 2021) (Fig. 12). By redshifting the SED fits and convolving them with the *Euclid* photometric filters (Fig. 13), we can empirically predict the flux densities of these protocluster galaxies expected in the VIS and NIR bands as a function of the redshift.

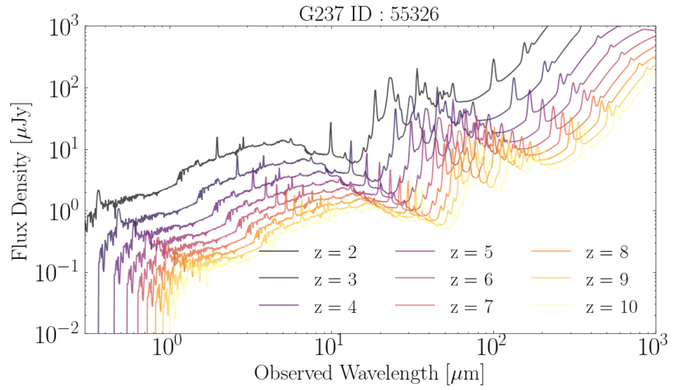

Fig. 13. The SED of the $z = 2.1576$ galaxy 55326 in G237 of Polletta et al. (2021) being redshifted up to $z = 10$. The flux densities in the observed *Euclid* bands SED are obtained at each redshift, and being compared to the surveys sensitivities.

Using 79 galaxies with redshifts confirmed spectroscopically from these samples for this process, and using the criterion of detecting at least 50% of those galaxies at a given redshift and at least in one *Euclid* band (usually H_{E}), we empirically find that the Euclid Wide Survey should allow us to detect galaxy protoclusters up to $z = 3$, and the Euclid Deep Survey up to $z = 5.5$. This empirical approach, however, does not address quantitatively the purity nor completeness of samples, but gives a useful first-order prediction.

The protoclusters we find here in the Q1 dataset at the Euclid Wide Survey depth are currently compatible in terms of redshift range with these empirical predictions, as well as with the predictions of Euclid Collaboration et al. (2025).

With the experience gained in this pilot project, we anticipate that using at least two algorithms in sequence, like DETECTIFz or MC-DTFE-LoG, and then PPM, increases the reliability of the detected protocluster search. Indeed, comparing each detection along the line of sight, especially the S/N and the photometric redshift of the overdensities, may be crucial to unveil fainter structures.

7. Conclusions

We search blindly in the *Euclid* Q1 data for galaxy protoclusters and find 81 overdensities. Focusing on the locations of *Planck* protocluster candidates, we detect seven protoclusters (plus four tentative detections) for which we estimate the photometric redshifts, lower limit for stellar masses, star-formation rates, and lower limits for the halo masses. At least two independent algorithms recovered the overdensities; for some sources, three algorithms were used and provided converging estimates.

Our detections are situated at redshifts $1.5 < z < 2.0$, slightly below the expected *Planck* selection and previous follow-up observations of *Planck* candidate protoclusters. However, it is worth noting that the protocluster-finder algorithm used in this study also outputs galaxy overdensities at lower S/N and higher redshift. At this stage, it is difficult to rule out the possibility that our current procedure selects primarily foreground line-of-sight overdensities more efficiently in the *Euclid* data than at higher redshift ($z > 2$). However, we favour a conservative approach and focus on the high reliability detections rather than choosing higher-redshift but lower S/N counterparts as the actual *Planck* protocluster candidates counterparts.

The *Euclid* protoclusters, counterparts of the *Planck* candidates, occupy an interesting location in the dark matter halo–mass, redshift plane $[\log_{10}(M_{\mathrm{h}}), z]$ (12.0–13.3, 1.5–2). The three best detected protoclusters lie above $M_{\mathrm{h}} > 10^{13} M_{\odot}$, while the four others lie around $M_{\mathrm{h}} \sim 3.10^{12} M_{\odot}$. A first search for counterparts of these *Euclid* protoclusters in the eROSITA and the South Pole Telescope (SPT) cluster catalogues shows no association. This suggests that the halos do not contain hot enough gas to emit in the X-rays or to cast shadows in the cosmic microwave background via the Sunyaev-Zel'dovich effect.

The estimated lower limits of M_{h} together with the photometric redshift range (towards the end of cosmic noon) probed and the star formation rates of the protoclusters raise several unanswered questions in this pilot project, among which: Is this set of seven protoclusters representative of the *Planck* protocluster candidate sample, as previous observations tend to detect higher-redshift higher SFR protoclusters, sometimes with a few structures along the line of sight ? Is this pilot program missing fainter galaxies in the overdensities, or higher redshift overdensities ? Are we witnessing the "protocluster dying phase" (or the protocluster swan song) ? Indeed we may expect the measured star-formation activity to be unsustainable, and thus witnessing the last star-forming event. What is the maturity of the detected protoclusters ? Do they contain gas and is which state is it?

Future observations and analyses in the millimetre w/ SPT, in the X-rays with eRosita or the XMM heritage programme Fornax, and optical/NIR/mm/radio spectroscopy will help to get a more clear view of these structures and on the thousands of protoclusters that will be detected in the forthcoming *Euclid* DR1 dataset.

Acknowledgements. We thank XXX and YYY for helpful comments on the manuscript. We thank L. Legrand for providing us with the stellar mass - halo mass relations electronically. We thank P. Behroozi and M. Shuntov for providing their relations online. T.D. acknowledges the support from CNES and from the Université Paris-Saclay. This work has been supported as part of France 2030 program ANR-11-IDEX-0003, attributed through the Astrophysical Axis of the Graduate School of Physics of the Université Paris-Saclay. M.P. acknowledges financial support from INAF mini-grant 2023 'Galaxy growth and fuelling in high-z structures'. The Euclid Consortium acknowledges the European Space Agency and a number of agencies and institutes that have supported the development of *Euclid*, in particular the Agenzia Spaziale Italiana, the Austrian Forschungsförderungsgesellschaft funded through BMK, the Belgian Science Policy, the Canadian Euclid Consortium, the Deutsches Zentrum für Luft- und Raumfahrt, the DTU Space and the Niels Bohr Institute in Denmark, the French Centre National d'Etudes Spatiales, the Fundação para a Ciência e a Tecnologia, the Hungarian Academy of Sciences, the Ministerio de Ciencia, Innovación y Universidades, the National Aeronautics and Space Administration, the National Astronomical Observatory of Japan, the Netherlandse Onderzoekschool Voor Astronomie, the Norwegian Space Agency, the Research Council of Finland, the Romanian Space Agency, the State Secretariat for Education, Research, and Innovation (SERI) at the Swiss Space Office (SSO), and the United Kingdom Space Agency. A complete and detailed list is available on the *Euclid* web site (`www.euclid-ec.org`). This work has made use of the *Euclid* Quick Release (Q1) data from the *Euclid* mission of the European Space Agency (ESA), 2025, `https://doi.org/10.57780/esa-2853f3b`.This paper made use of the *Planck* data publicly available at `https://www.esa.int/Planck`. *Planck* is a project of the European Space Agency (ESA) with instruments provided by two scientific consortia funded by ESA member states and led by Principal Investigators from France and Italy, telescope reflectors provided through a collaboration between ESA and a scientific consortium led and funded by Denmark, and additional contributions from NASA (USA). The *Herschel* spacecraft was designed, built, tested, and launched under a contract to ESA managed by the *Herschel*/*Planck* Project team by an industrial consortium under the overall responsibility of the prime contractor Thales Alenia Space (Cannes), and including Astrium (Friedrichshafen) responsible for the payload module and for system testing at spacecraft level, Thales Alenia Space (Turin) responsible for the service module, and Astrium (Toulouse) responsible for the telescope, with in excess of a hundred subcontractors.

References

Aihara, H., Arimoto, N., Armstrong, R., et al. 2018, PASJ, 70, S4

Alberts, S. & Noble, A. 2022, Universe, 8, 554
Albrecht, A., Bernstein, G., Cahn, R., et al. 2006, arXiv e-prints, astro
Andreon, S., Newman, A. B., Trinchieri, G., et al. 2014, A&A, 565, A120
Aussel, H. et al. 2025, A&A, hopefully submitted
Behroozi, P., Wechsler, R. H., Hearin, A. P., & Conroy, C. 2019, MNRAS, 488, 3143
Behroozi, P. S., Wechsler, R. H., & Conroy, C. 2013, ApJ, 770, 57
Bisigello, L., Kuchner, U., Conselice, C. J., et al. 2020, MNRAS, 494, 2337
Calvi, R., Castignani, G., & Dannerbauer, H. 2023, A&A, 678, A15
Calvi, R., Dannerbauer, H., Arrabal Haro, P., et al. 2021, MNRAS, 502, 4558
Casey, C. M. 2012, MNRAS, 425, 3094
Casey, C. M. 2016, ApJ, 824, 36
Casey, C. M., Cooray, A., Capak, P., et al. 2015, ApJ, 808, L33
Castignani, G., Chiaberge, M., Celotti, A., & Norman, C. 2014a, ApJ, 792, 113
Castignani, G., Chiaberge, M., Celotti, A., Norman, C., & De Zotti, G. 2014b, ApJ, 792, 114
Castignani, G., Combes, F., Salomé, P., et al. 2019, A&A, 623, A48
Champagne, J. B., Casey, C. M., Zavala, J. A., et al. 2021, ApJ, 913, 110
Chapman, S. C., Blain, A., Ibata, R., et al. 2009, ApJ, 691, 560
Cheng, T., Clements, D. L., Greenslade, J., et al. 2019, MNRAS, 490, 3840
Cheng, T., Clements, D. L., Greenslade, J., et al. 2020, MNRAS, 494, 5985
Clements, D. L., Braglia, F., Petitpas, G., et al. 2016, MNRAS, 461, 1719
Clements, D. L., Braglia, F. G., Hyde, A. K., et al. 2014, MNRAS, 439, 1193
Coogan, R. T., Daddi, E., Sargent, M. T., et al. 2018, MNRAS, 479, 703
Cortese, L., Fritz, J., Bianchi, S., et al. 2014, MNRAS, 440, 942
Daddi, E., Delvecchio, I., Dimauro, P., et al. 2022, A&A, 661, L7
Darvish, B., Scoville, N. Z., Martin, C., et al. 2020, ApJ, 892, 8
Dekel, A. & Birnboim, Y. 2006, MNRAS, 368, 2
Diener, C., Lilly, S. J., Ledoux, C., et al. 2015, ApJ, 802, 31
Emonts, B. H. C., Cai, Z., Prochaska, J. X., Li, Q., & Lehnert, M. D. 2019, ApJ, 887, 86
Euclid Collaboration, Böhringer, H., Chon, G., et al. 2025, A&A, 693, A59
Euclid Collaboration: Cropper, M., Al Bahlawan, A., Amiaux, J., et al. 2024, A&A, accepted, arXiv:2405.13492
Euclid Collaboration: Jahnke, K., Gillard, W., Schirmer, M., et al. 2024, A&A, accepted, arXiv:2405.13493
Euclid Collaboration: McCracken, H. et al. 2025, A&A, hopefully submitted
Euclid Collaboration: Mellier, Y., Abdurro'uf, Acevedo Barroso, J., et al. 2024, A&A, accepted, arXiv:2405.13491
Euclid Collaboration: Polenta, G. et al. 2025, A&A, hopefully submitted
Euclid Collaboration: Romelli, E., Kuemmel, M., Dole, H., et al. 2025, A&A, hopefully submitted
Euclid Collaboration: Scaramella, R., Amiaux, J., Mellier, Y., et al. 2022, A&A, 662, A112
Euclid Collaboration: Tucci, M., Paltani, S., Hartley, W., et al. 2025, A&A, hopefully submitted
Euclid Quick Release Q1. 2025, https://doi.org/10.57780/esa-2853f3b
Flores-Cacho, I., Pierini, D., Soucail, G., et al. 2016, A&A, 585, A54
Gatica, C., Demarco, R., Dole, H., et al. 2024, MNRAS, 527, 3006
Girelli, G., Pozzetti, L., Bolzonella, M., et al. 2020, A&A, 634, A135
Gobat, R., Strazzullo, V., Daddi, E., et al. 2013, ApJ, 776, 9
Gómez-Guijarro, C., Riechers, D. A., Pavesi, R., et al. 2019, ApJ, 872, 117
Gómez-Guijarro, C., Toft, S., Karim, A., et al. 2018, ApJ, 856, 121
Gouin, C., Aghanim, N., Dole, H., Polletta, M., & Park, C. 2022, A&A, 664, A155
Greenslade, J., Clements, D. L., Cheng, T., et al. 2018, MNRAS, 476, 3336
Griffin, M. J., Abergel, A., Abreu, A., et al. 2010, A&A, 518, L3
Hill, R., Polletta, M. d. C., Bethermin, M., et al. 2024, arXiv e-prints, arXiv:2412.00294
Ivison, R. J., Smail, I., Amblard, A., et al. 2012, MNRAS, 425, 1320
Johnson, B. D., Leja, J., Conroy, C., & Speagle, J. S. 2021, ApJS, 254, 22
Kennicutt, R. C. & Evans, N. J. 2012, ARA&A, 50, 531
Kneissl, R., Polletta, M. d. C., Martinache, C., et al. 2019, A&A, 625, A96
Kotulla, R., Fritze, U., Weilbacher, P., & Anders, P. 2009, MNRAS, 396, 462
Koyama, Y., Kodama, T., Tadaki, K.-i., et al. 2013, MNRAS, 428, 1551
Koyama, Y., Polletta, M. d. C., Tanaka, I., et al. 2021, MNRAS, 503, L1
Kubo, M., Toshikawa, J., Kashikawa, N., et al. 2019, ApJ, 887, 214
Kubo, M., Yamada, T., Ichikawa, T., et al. 2015, ApJ, 799, 38
Lammers, C., Hill, R., Lim, S., et al. 2022, MNRAS, 514, 5004
Laporte, N., Zitrin, A., Dole, H., et al. 2022, A&A, 667, L3
Legrand, L., McCracken, H. J., Davidzon, I., et al. 2019, MNRAS, 486, 5468
Li, Q., Conselice, C. J., Sarron, F., et al. 2024, arXiv e-prints, arXiv:2405.17359
Lindeberg, T. 1992, Journal of Mathematical Imaging and Vision, 1, 65
Long, A. S., Cooray, A., Ma, J., et al. 2020, ApJ, 898, 133
MacKenzie, T. P., Scott, D., Bianconi, M., et al. 2017, MNRAS, 468, 4006
Madau, P. & Dickinson, M. 2014, ARA&A, 52, 415
Martig, M., Bournaud, F., Teyssier, R., & Dekel, A. 2009, ApJ, 707, 250
Martinache, C., Rettura, A., Dole, H., et al. 2018, A&A, 620, A198
Miller, T. B., Chapman, S. C., Aravena, M., et al. 2018, Nature, 556, 469
Morishita, T., Liu, Z., Stiavelli, M., et al. 2024, arXiv e-prints, arXiv:2408.10980
Morishita, T., Roberts-Borsani, G., Treu, T., et al. 2023, ApJ, 947, L24
Negrello, M., Gonzalez-Nuevo, J., De Zotti, G., et al. 2017, MNRAS, 470, 2253
Nelson, D., Springel, V., Pillepich, A., et al. 2019, Computational Astrophysics and Cosmology, 6, 2
Nicastro, F., Kaastra, J., Krongold, Y., et al. 2018, Nature, 558, 406
Oliver, S. J., Bock, J., Altieri, B., et al. 2012, MNRAS, 424, 1614
Oteo, I., Ivison, R. J., Dunne, L., et al. 2018, ApJ, 856, 72
Overzier, R. A. 2016, A&A Rev., 24, 14
Pérez-Martínez, J. M., Dannerbauer, H., Emonts, B. H. C., et al. 2024a, arXiv e-prints, arXiv:2411.12138
Pérez-Martínez, J. M., Kodama, T., Koyama, Y., et al. 2024b, MNRAS, 527, 10221
Pillepich, A., Springel, V., Nelson, D., et al. 2018, MNRAS, 473, 4077
Planck Collaboration, Ade, P. A. R., Aghanim, N., et al. 2015a, A&A, 581, A14
Planck Collaboration, Ade, P. A. R., Aghanim, N., et al. 2016, A&A, 596, A100
Planck Collaboration, Aghanim, N., Akrami, Y., et al. 2020a, A&A, 641, A1
Planck Collaboration, Aghanim, N., Akrami, Y., et al. 2020b, A&A, 641, A6
Planck Collaboration, Aghanim, N., Altieri, B., et al. 2015b, A&A, 582, A30
Pokhrel, R., Gutermuth, R., Ali, B., et al. 2016, MNRAS, 461, 22
Polletta, M., Dole, H., Martinache, C., et al. 2022, A&A, 662, A85
Polletta, M., Frye, B. L., Garuda, N., et al. 2024, A&A, 690, A285
Polletta, M., Soucail, G., Dole, H., et al. 2021, A&A, 654, A121
Popescu, R., Pope, A., Lee, K.-S., et al. 2023, ApJ, 958, 12
Ramos Chernenko, N., Bonjean, V., Dannerbauer, H., Gutiérrez de La Cruz, C., & Cucciati, O. 2024, in EAS2024, European Astronomical Society Annual Meeting, 2014
Ramos Chernenko, N. et al. 2025, A&A, hopefully submitted
Remus, R.-S., Dolag, K., & Dannerbauer, H. 2023, ApJ, 950, 191
Roseboom, I. G., Oliver, S. J., Kunz, M., et al. 2010, MNRAS, 409, 48
Rotermund, K. M., Chapman, S. C., Phadke, K. A., et al. 2021, MNRAS, 502, 1797
Sarron, F. & Conselice, C. J. 2021, MNRAS, 506, 2136
Schaap, W. E. 2007, PhD thesis, University of Groningen, Netherlands
Schaap, W. E. & van de Weygaert, R. 2000, A&A, 363, L29
Schawinski, K., Urry, C. M., Simmons, B. D., et al. 2014, MNRAS, 440, 889
Schreiber, C., Pannella, M., Elbaz, D., et al. 2015, A&A, 575, A74
Shi, K., Huang, Y., Lee, K.-S., et al. 2019, ApJ, 879, 9
Shimakawa, R., Pérez-Martínez, J. M., Dannerbauer, H., et al. 2024, ApJ, 977, 73
Shuntov, M., McCracken, H. J., Gavazzi, R., et al. 2022, A&A, 664, A61
Sillassen, N. B., Jin, S., Magdis, G. E., et al. 2024, A&A, 690, A55
Smith, A. J., Wang, L., Oliver, S. J., et al. 2012, MNRAS, 419, 377
Soifer, B. T., Helou, G., & Werner, M. 2008, ARA&A, 46, 201
Sotak, G. & Boyer, K. 1989, Computer Vision, Graphics, and Image Processing, 48, 147
Stanford, S. A., Brodwin, M., Gonzalez, A. H., et al. 2012, ApJ, 753, 164
Steidel, C. C., Adelberger, K. L., Shapley, A. E., et al. 2000, ApJ, 532, 170
Strazzullo, V., Pannella, M., Mohr, J. J., et al. 2023, A&A, 669, A131
Tadaki, K.-i., Kodama, T., Hayashi, M., et al. 2019, PASJ, 71, 40
van der Burg, R. F. J., Muzzin, A., Hoekstra, H., et al. 2014, A&A, 561, A79
Wang, T., Elbaz, D., Daddi, E., et al. 2016, ApJ, 828, 56
Werner, M. W., Roellig, T. L., Low, F. J., et al. 2004, ApJS, 154, 1
Willis, J. P., Canning, R. E. A., Noordeh, E. S., et al. 2020, Nature, 577, 39
Windhorst, R. A., Cohen, S. H., Jansen, R. A., et al. 2023, AJ, 165, 13

[1] Université Paris-Saclay, CNRS, Institut d'astrophysique spatiale, 91405, Orsay, France
[2] IRAP
[3] INAF-OAS Bologna
[4] Instituto de Astrofísica de Canarias
[5] Université Paris-Saclay, CEA, DEDIP, 91191, Gif-sur-Yvette, France
[6] Université Paris-Saclay, CNRS, INRIA Paris-Saclay, LISN, France
[7] Department of Astronomy/Steward Observatory, University of Arizona, 933 N. Cherry Avenue, Tucson, AZ, 85721, USA
[8] INAF - Istituto di Astrofisica Spaziale e Fisica Cosmica di Milano, via A. Corti 12, I-20133 Milan, Italy
[9] Department of Physics and Center for Astrophysics and Space Science, University of California at San Diego, 9500 Gilman Drive, La Jolla, CA 92093, USA
[10] Department of Physics and Astronomy, University of British Columbia, Vancouver, BC V6T 1Z1, Canada

Appendix A: *Euclid* VIS images at the location of *Planck* protocluster candidates

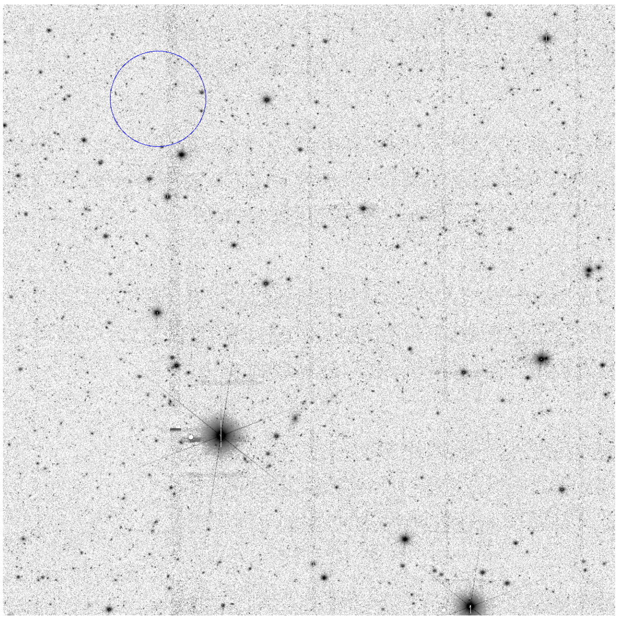

Fig. A.1. *Euclid* VIS tile 10202059 (covering $30' \times 30'$) with the *Planck* protocluster candidate PLCK_XXXXXX shown as a circle of radius $2\farcm5$ (while the *Planck* beam has a diameter of about $5'$) in EDF-S.

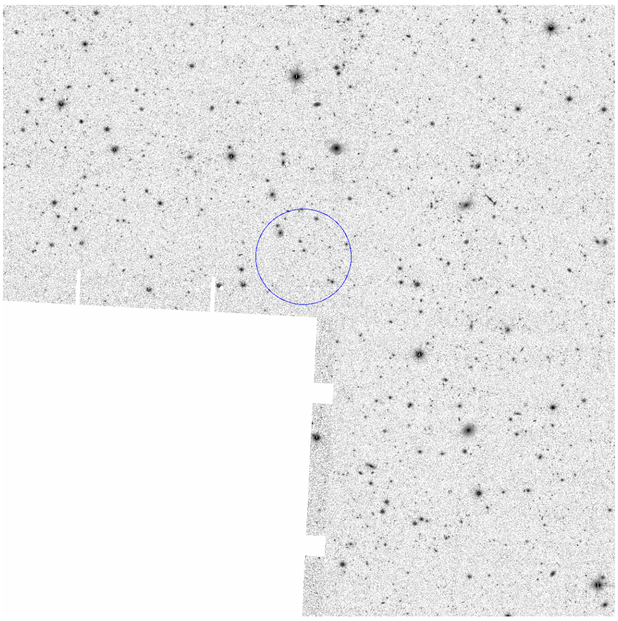

Fig. A.2. *Euclid* VIS tile 10202065 (covering $30' \times 30'$) with the *Planck* protocluster candidate PLCK_XXXXXX shown as a circle of radius $2\farcm5$ (while the *Planck* beam has a diameter of about $5'$) in EDF-S.

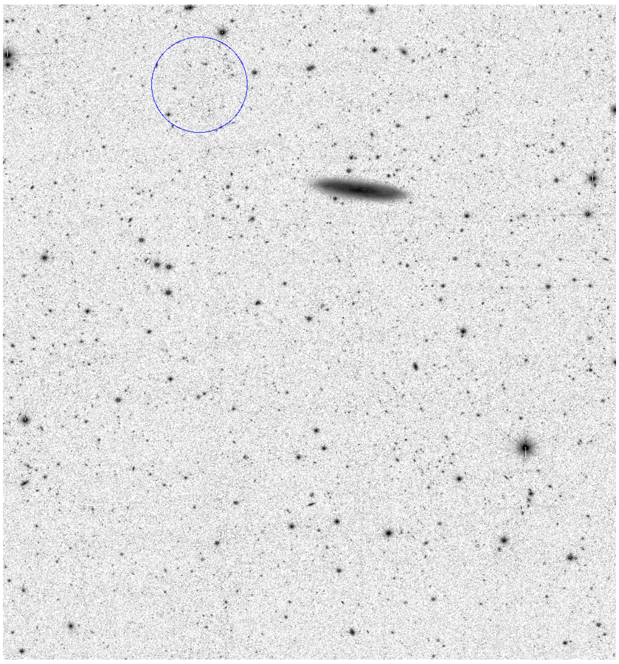

Fig. A.3. *Euclid* VIS tile 102020530 (covering $30' \times 30'$) with the *Planck* protocluster candidate PLCK_XXXXXX shown as a circle of radius $2\farcm5$ (while the *Planck* beam has a diameter of about $5'$) in EDF-S.

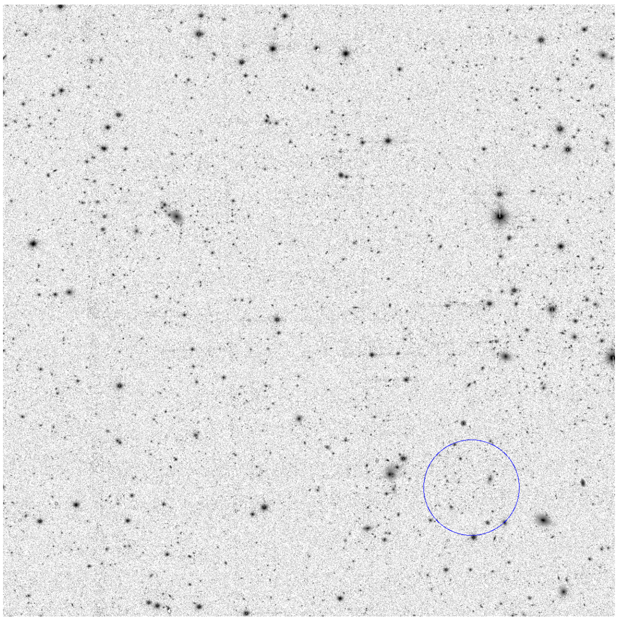

Fig. A.4. *Euclid* VIS tile 102021010 (covering $30' \times 30'$) with the *Planck* protocluster candidate PLCK_XXXXXX shown as a circle of radius $2\farcm5$ (while the *Planck* beam has a diameter of about $5'$) in EDF-S.

Appendix B: Five *Euclid* DETECTIFz detections of protoclusters at the *Planck* locations

Appendix C: *Euclid* Four DETECTIFz tentative detections of protoclusters at the *Planck* locations

Appendix D: Detected protoclusters

Table C.1. Tentative detections of *Euclid* protoclusters with DETECTIFz at the location of *Planck* & *Herschel* protocluster candidates.

Planck field name	MER Tile number	ID	$z_{\rm ph}$	N Gal	S/N	Overdensity $\log_{10}[1+\delta]$	$M_\star$ tot $\log_{10}[M_\odot]$	SFR tot $\log_{10}[M_\odot\,{\rm yr}^{-1}]$
G222.05-54.24	102 045 467	28	$1.45^{+0.14}_{-0.09}$	3	1.93	0.21	$10.68^{+0.08}_{-0.15}$	$1.92^{+0.13}_{-0.34}$
G222.75-55.98	102 044 821	4	$2.22^{+0.20}_{-0.30}$	3	2.90	0.31	$12.87^{+0.15}_{-0.19}$	$2.69^{+0.17}_{-0.28}$
G257.13-49.16	102 021 010	0	$2.70^{+0.51}_{-0.32}$	2	10	0.41	$9.99^{+0.20}_{-0.18}$	$1.14^{+0.10}_{-0.08}$
G257.71-47.99	102 020 059	14	$1.94^{+0.2}_{-0.16}$	2	2.84	0.26	$10.71^{+0.21}_{-0.17}$	$2.69^{+0.1}_{-0.81}$

Table D.1. Coordinates of detected protoclusters

Euclid Deep Field	*Planck* field name	*Euclid* DETECTIFz ID	RA (deg)	Dec (deg)	Ref. table
EDF-F	G221.09-54.59	11	52.722	−26.404	3
EDF-F	G222.05-54.24	28	53.184	−26.888	C.1
EDF-F	G222.75-55.98	16	51.273	−27.559	3
EDF-F	G222.75-55.98	4	51.259	−27.602	C.1
EDF-F	G224.36-53.19	7	54.556	−28.122	3
EDF-S	G257.13-49.16	0	58.183	−48.668	C.1
EDF-S	G254.49-47.73	6	60.699	−47.283	2
EDF-S	G254.49-47.73	14	60.848	−47.456	3
EDF-S	G254.49-47.73	17	60.796	−47.309	3
EDF-S	G257.71-47.99	14	59.704	−49.296	C.1
EDF-S	G257.01-45.18	0	64.012	−49.409	2

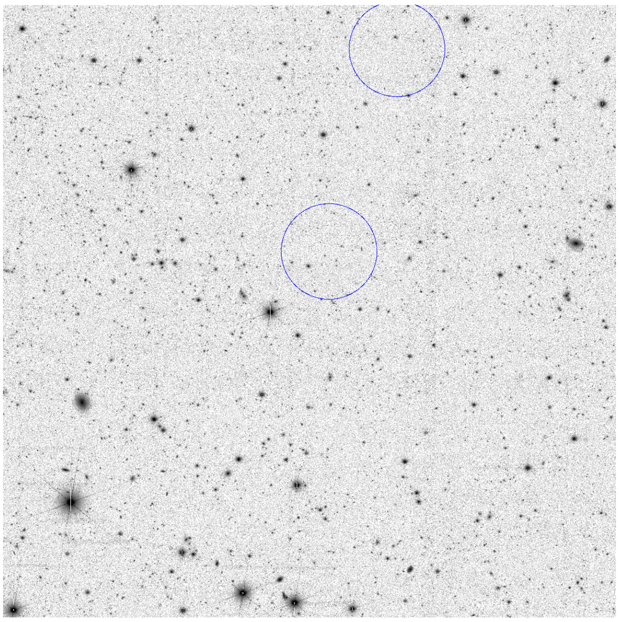

Fig. A.5. *Euclid* VIS tile 102021984 (covering 30′ × 30′) with two *Planck* protocluster candidates PLCK_XXXXXX and PLCK_XXXXXX shown as a circles of radius 2.′5 (while the *Planck* beam has a diameter of about 5′) in EDF-S.

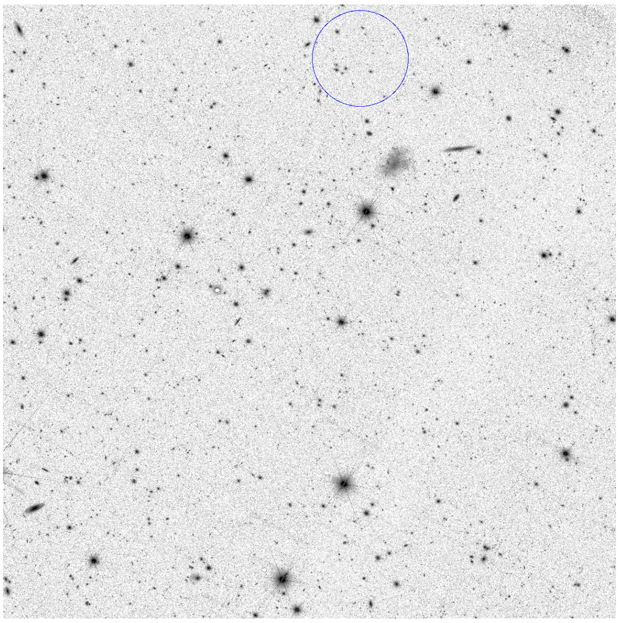

Fig. A.6. *Euclid* VIS tile 102023474 (covering 30′ × 30′) with two *Planck* protocluster candidates PLCK_XXXXXX and PLCK_XXXXXX shown as a circles of radius 2.′5 (while the *Planck* beam has a diameter of about 5′) in EDF-S.

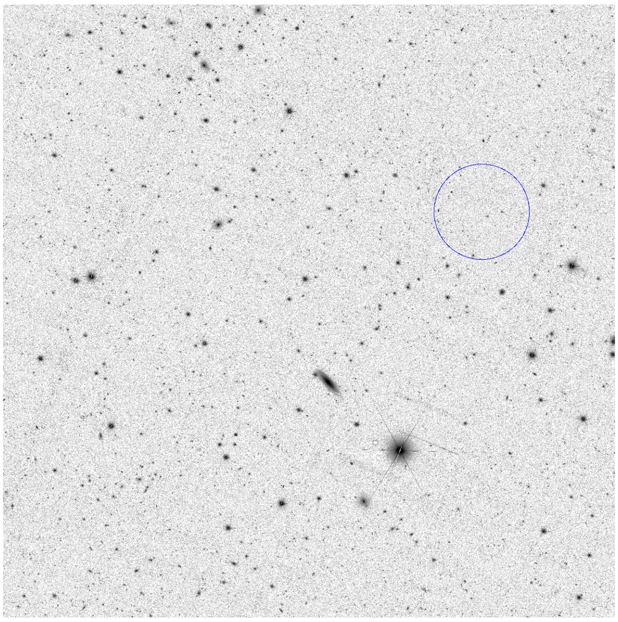

Fig. A.7. *Euclid* VIS tile 1020246112 (covering 30′ × 30′) with the *Planck* protocluster candidate PLCK_XXXXXX shown as a circle of radius 2′.5 (while the *Planck* beam has a diameter of about 5′) in EDF-F.

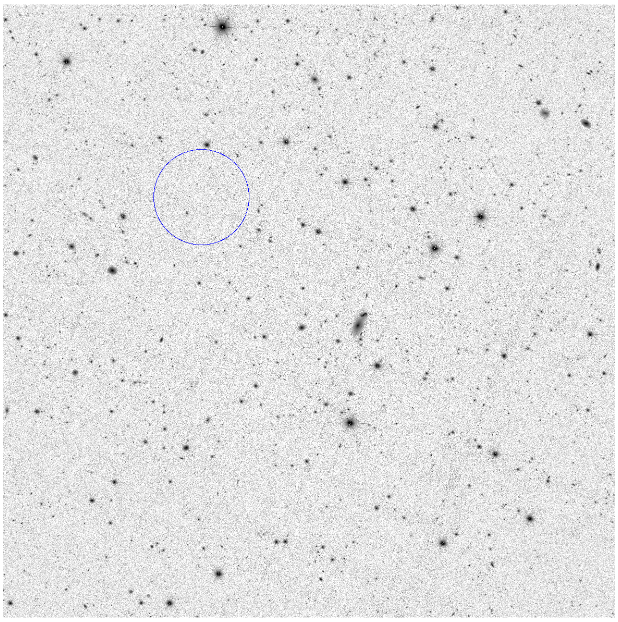

Fig. A.8. *Euclid* VIS tile 1020245467 (covering 30′ × 30′) with the *Planck* protocluster candidate PLCK_XXXXXX shown as a circle of radius 2′.5 (while the *Planck* beam has a diameter of about 5′) in EDF-F.

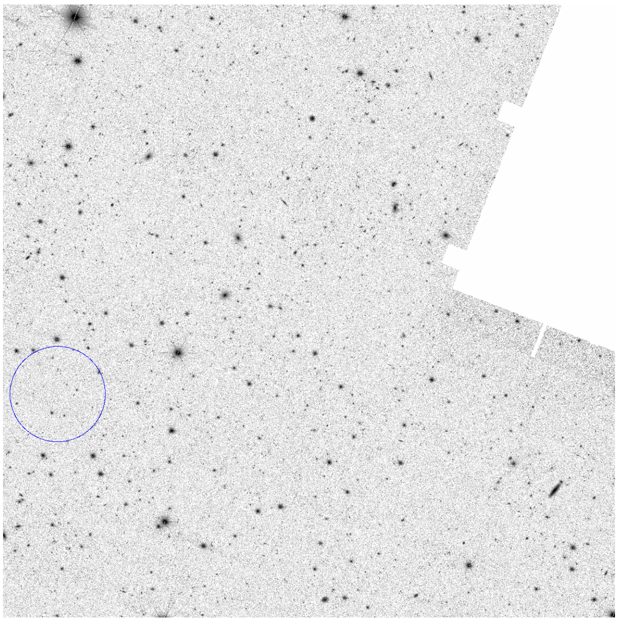

Fig. A.9. *Euclid* VIS tile 1020244821 (covering 30′ × 30′) with the *Planck* protocluster candidate PLCK_XXXXXX shown as a circle of radius 2′.5 (while the *Planck* beam has a diameter of about 5′) in EDF-F.

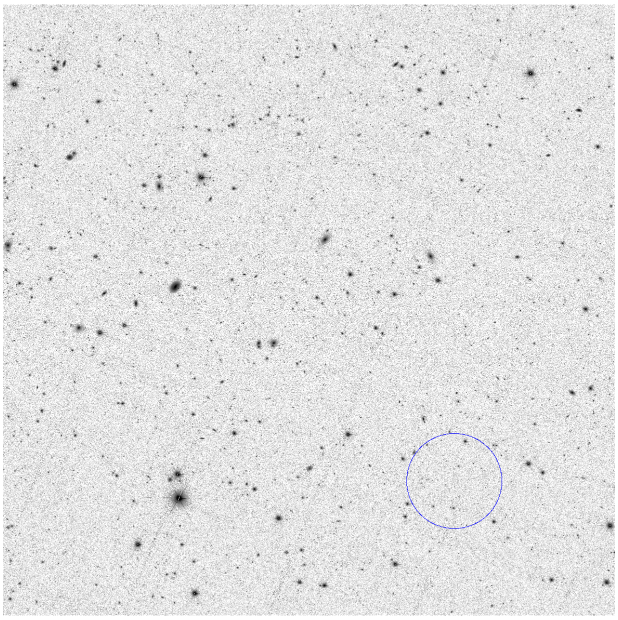

Fig. A.10. *Euclid* VIS tile 1020244824 (covering 30′ × 30′) with the *Planck* protocluster candidate PLCK_XXXXXX shown as a circle of radius 2′.5 (while the *Planck* beam has a diameter of about 5′) in EDF-F.

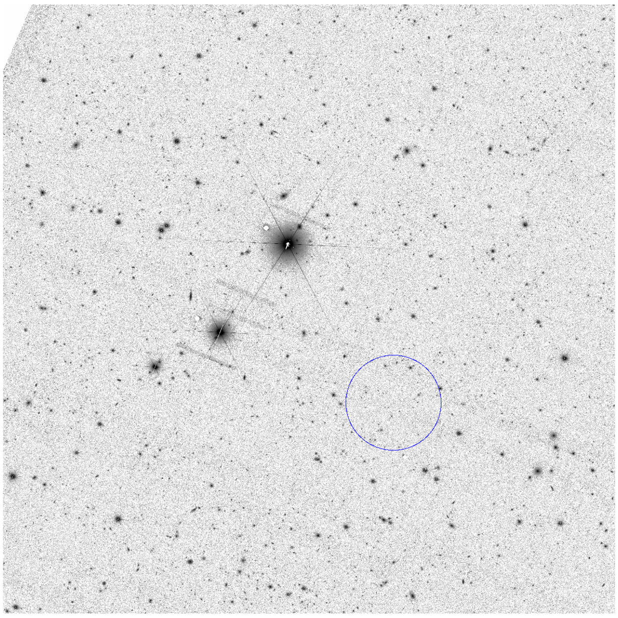

Fig. A.11. *Euclid* VIS tile 1020244188 (covering $30' \times 30'$) with the *Planck* protocluster candidate PLCK_XXXXXX shown as a circle of radius $2\overset{\prime}{.}5$ (while the *Planck* beam has a diameter of about $5'$) in EDF-F.

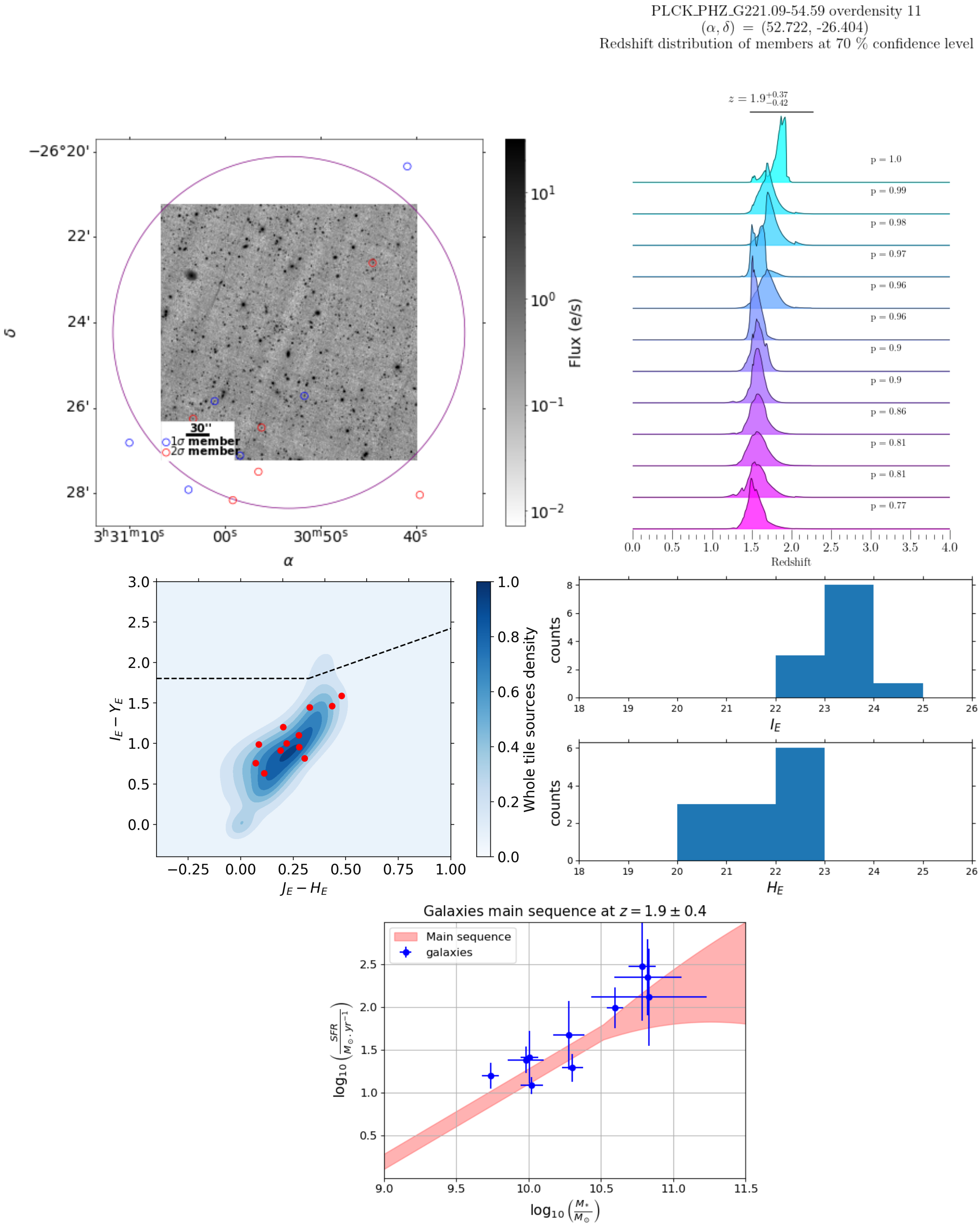

Fig. B.1. *Euclid* protocluster detected by DETECTIFz: NIR $H_{\rm E}$ image; Photometric redshifts; colour-colour plot; histograms of VIS $I_{\rm E}$ and NIR $H_{\rm E}$ magnitudes. Star-formation rate (SFR) vs. stellar mass ($M_\star$) of galaxies. The main sequence of Schreiber et al. (2015) is overploted in red.

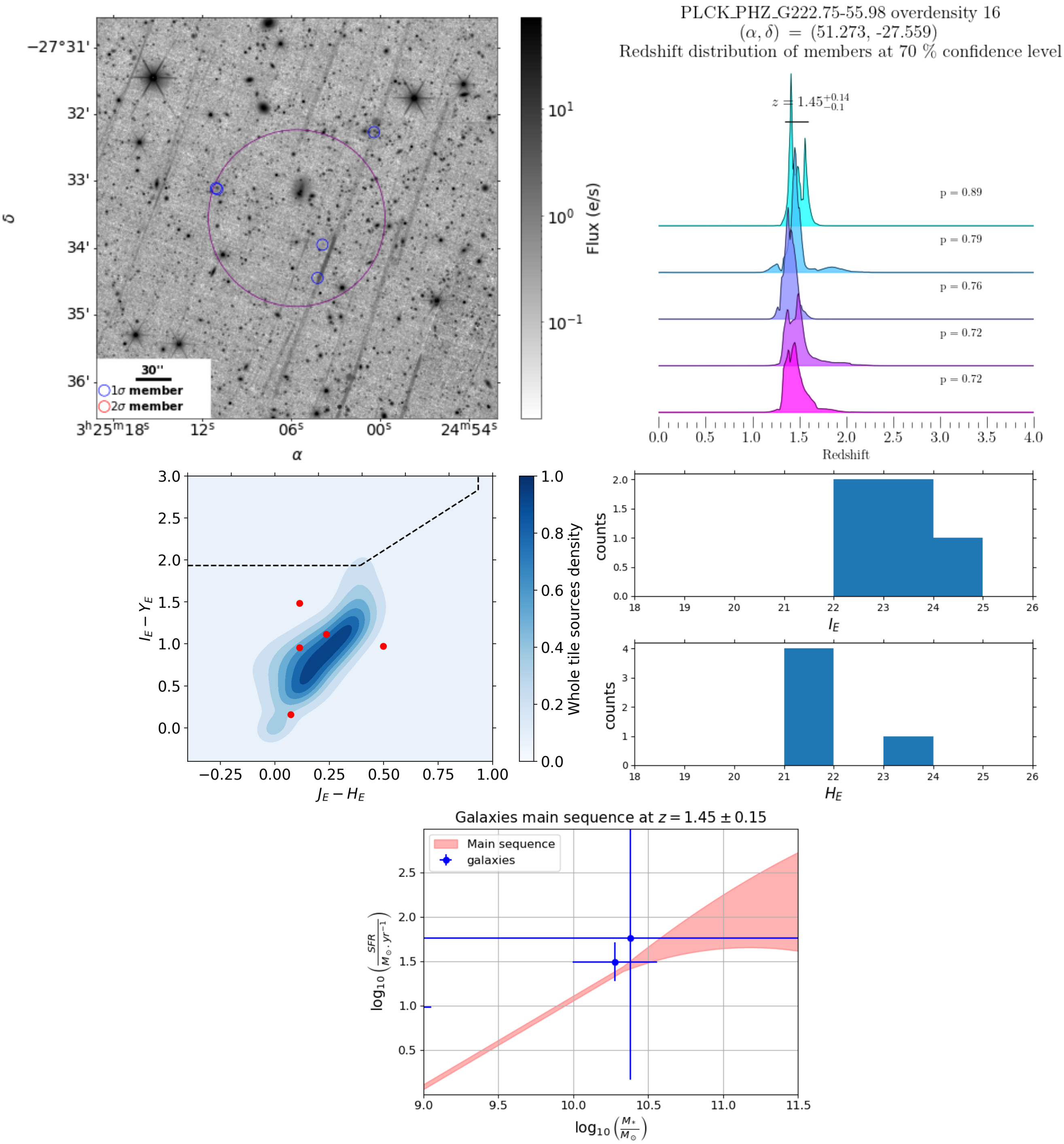

Fig. B.2. *Euclid* protocluster detected by DETECTIFz: NIR $H_{\rm E}$ image; Photometric redshifts; colour-colour plot; histograms of VIS $I_{\rm E}$ and NIR $H_{\rm E}$ magnitudes. Star-formation rate (SFR) vs. stellar mass ($M_\star$) of galaxies. The main sequence of Schreiber et al. (2015) is overploted in red.

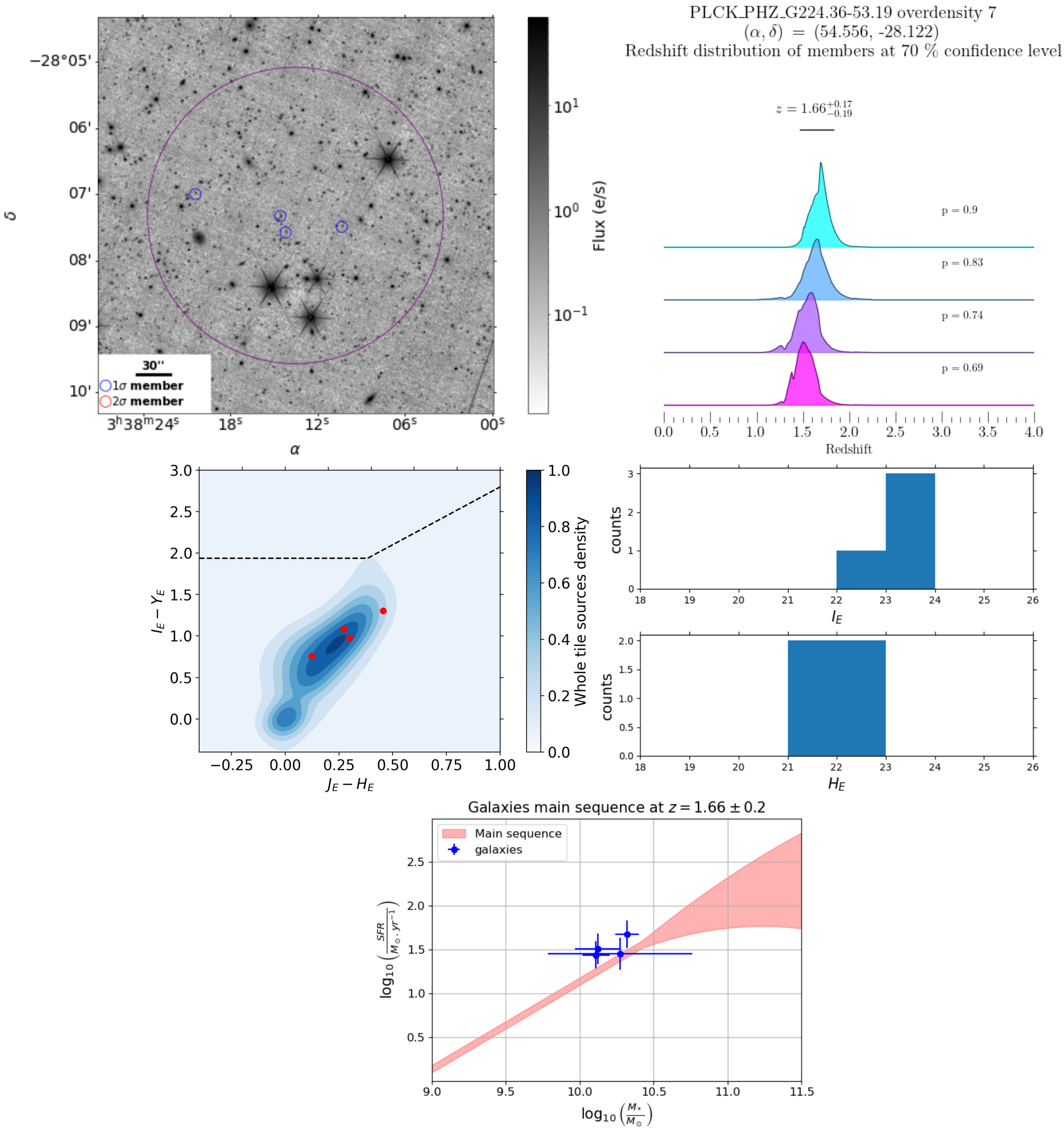

Fig. B.3. *Euclid* protocluster detected by DETECTIFz: NIR $H_{\rm E}$ image; Photometric redshifts; colour-colour plot; histograms of VIS $I_{\rm E}$ and NIR $H_{\rm E}$ magnitudes. Star-formation rate (SFR) vs. stellar mass ($M_\star$) of galaxies. The main sequence of Schreiber et al. (2015) is overploted in red.

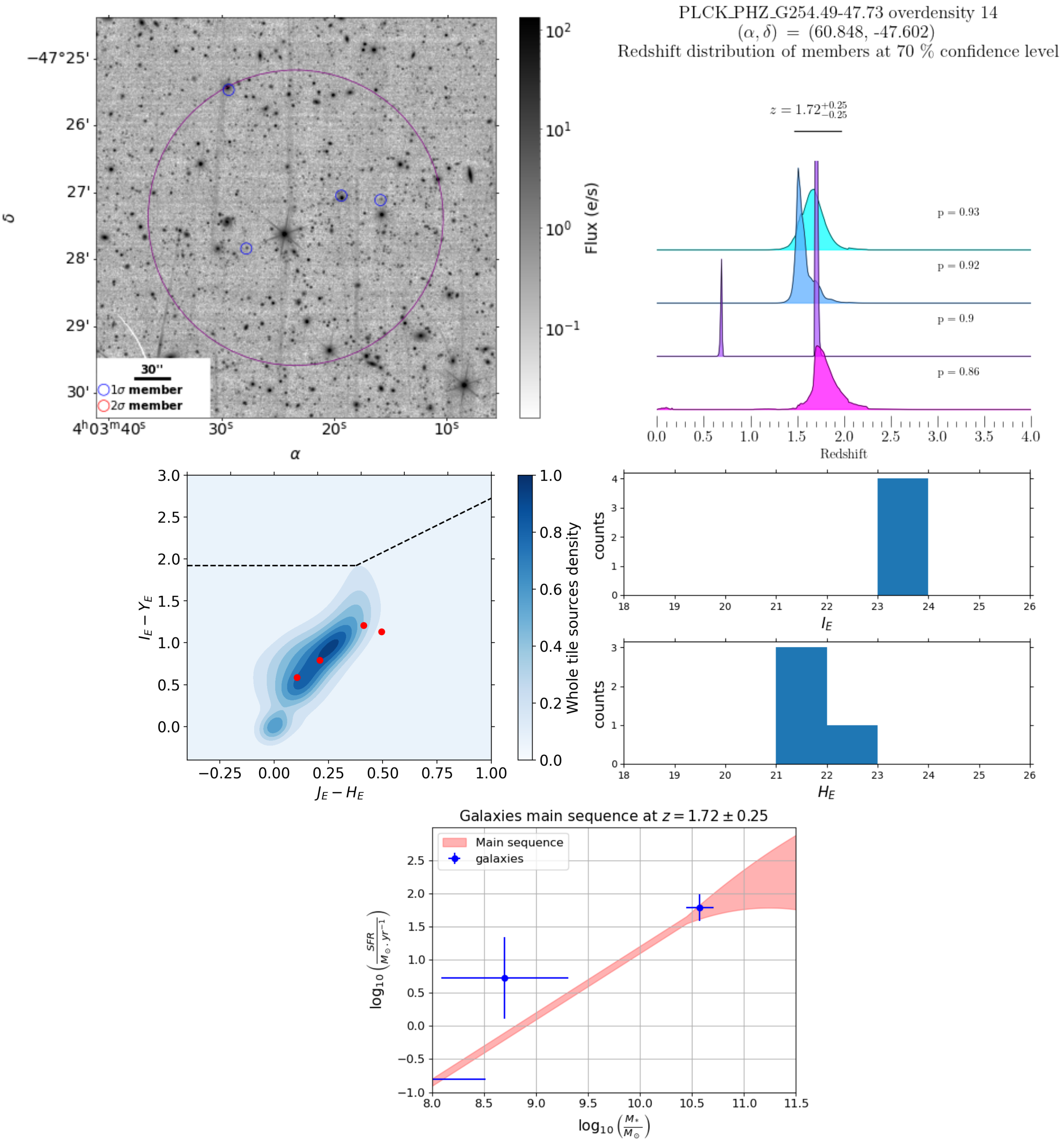

Fig. B.4. *Euclid* protocluster detected by DETECTIFz: NIR H_{E} image; Photometric redshifts; colour-colour plot; histograms of VIS I_{E} and NIR H_{E} magnitudes. Star-formation rate (SFR) vs. stellar mass ($M_{\star}$) of galaxies. The main sequence of Schreiber et al. (2015) is overploted in red.

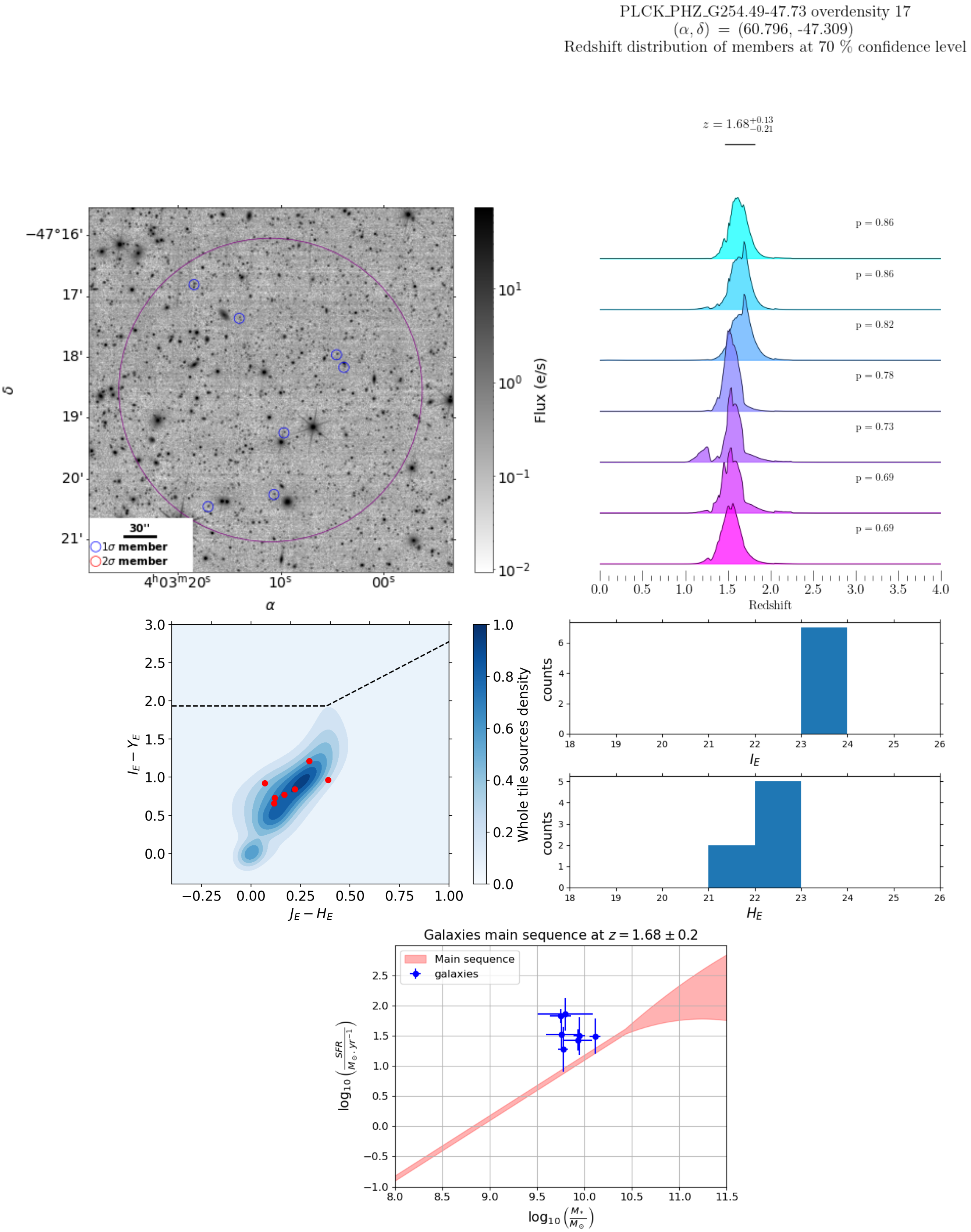

Fig. B.5. *Euclid* protocluster detected by DETECTIFz: NIR H_{E} image; Photometric redshifts; colour-colour plot; histograms of VIS I_{E} and NIR H_{E} magnitudes. Star-formation rate (SFR) vs. stellar mass ($M_{\star}$) of galaxies. The main sequence of Schreiber et al. (2015) is overploted in red.

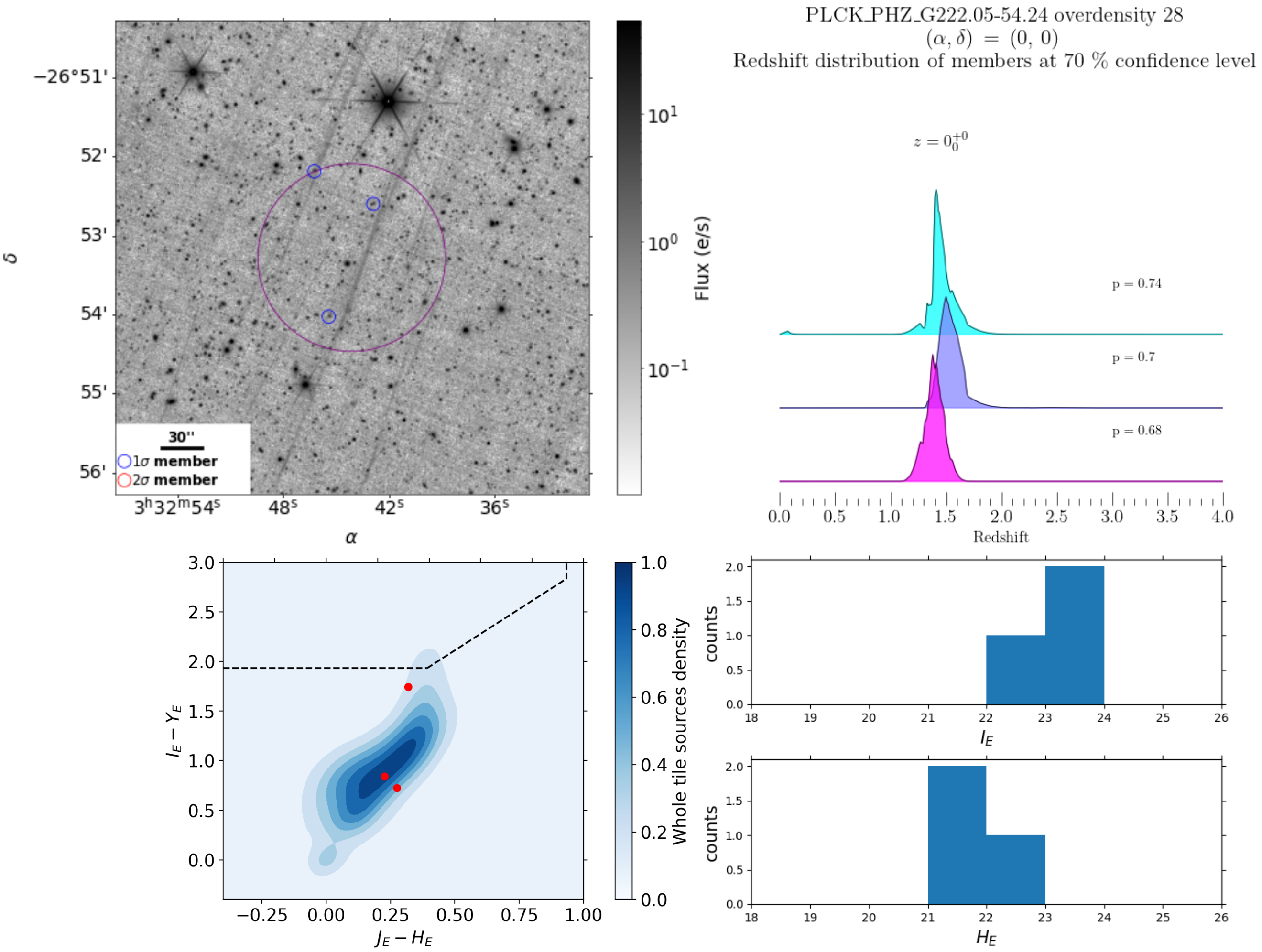

Fig. C.1. *Euclid* protocluster detected by DETECTIFz: NIR H_{E} image; Photometric redshifts; colour-colour plot; histograms of VIS I_{E} and NIR H_{E} magnitudes.

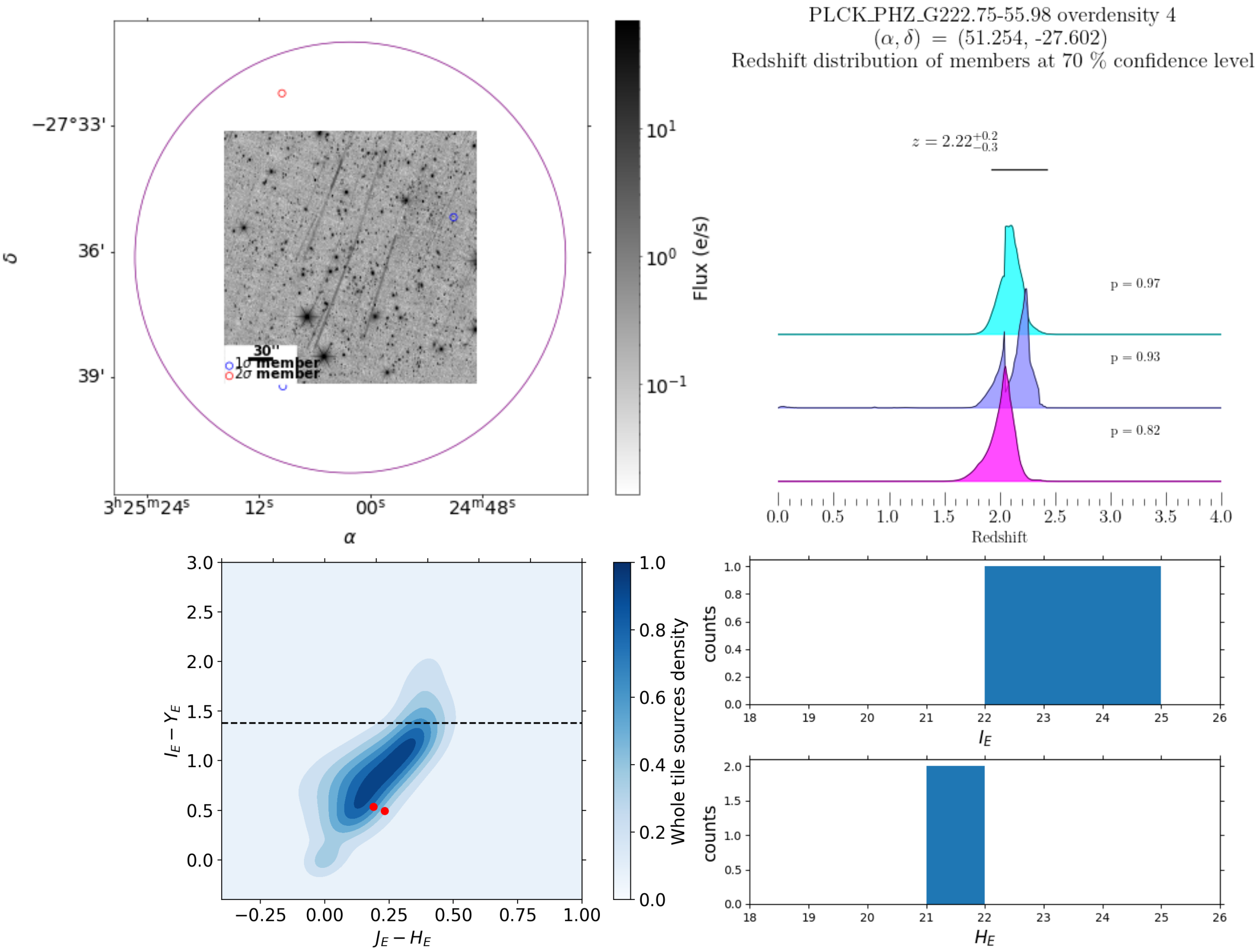

Fig. C.2. *Euclid* protocluster detected by DETECTIFz: NIR H_{E} image; Photometric redshifts; colour-colour plot; histograms of VIS I_{E} and NIR H_{E} magnitudes.

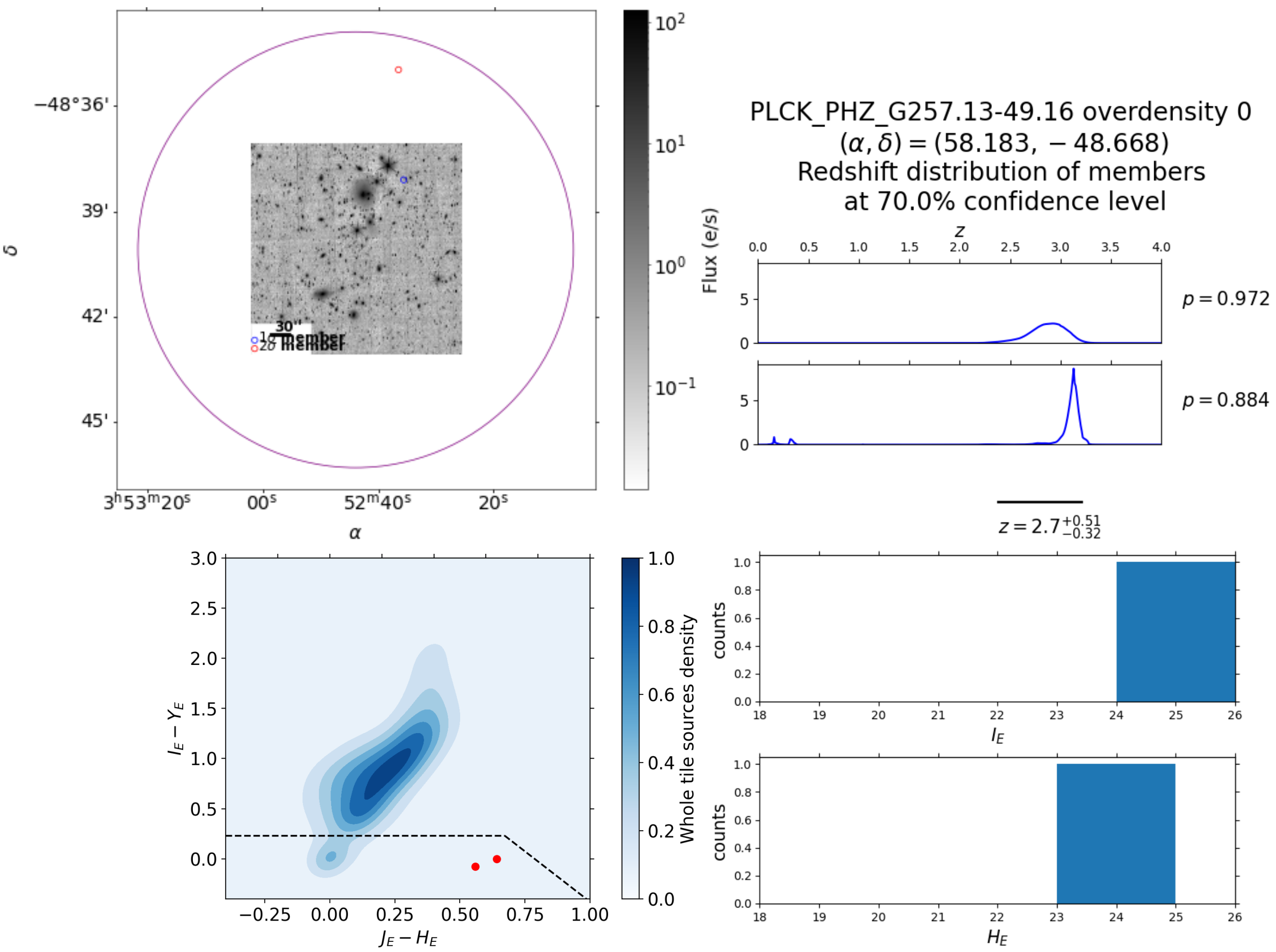

Fig. C.3. *Euclid* protocluster detected by DETECTIFz: NIR H_{E} image; Photometric redshifts; colour-colour plot; histograms of VIS I_{E} and NIR H_{E} magnitudes.

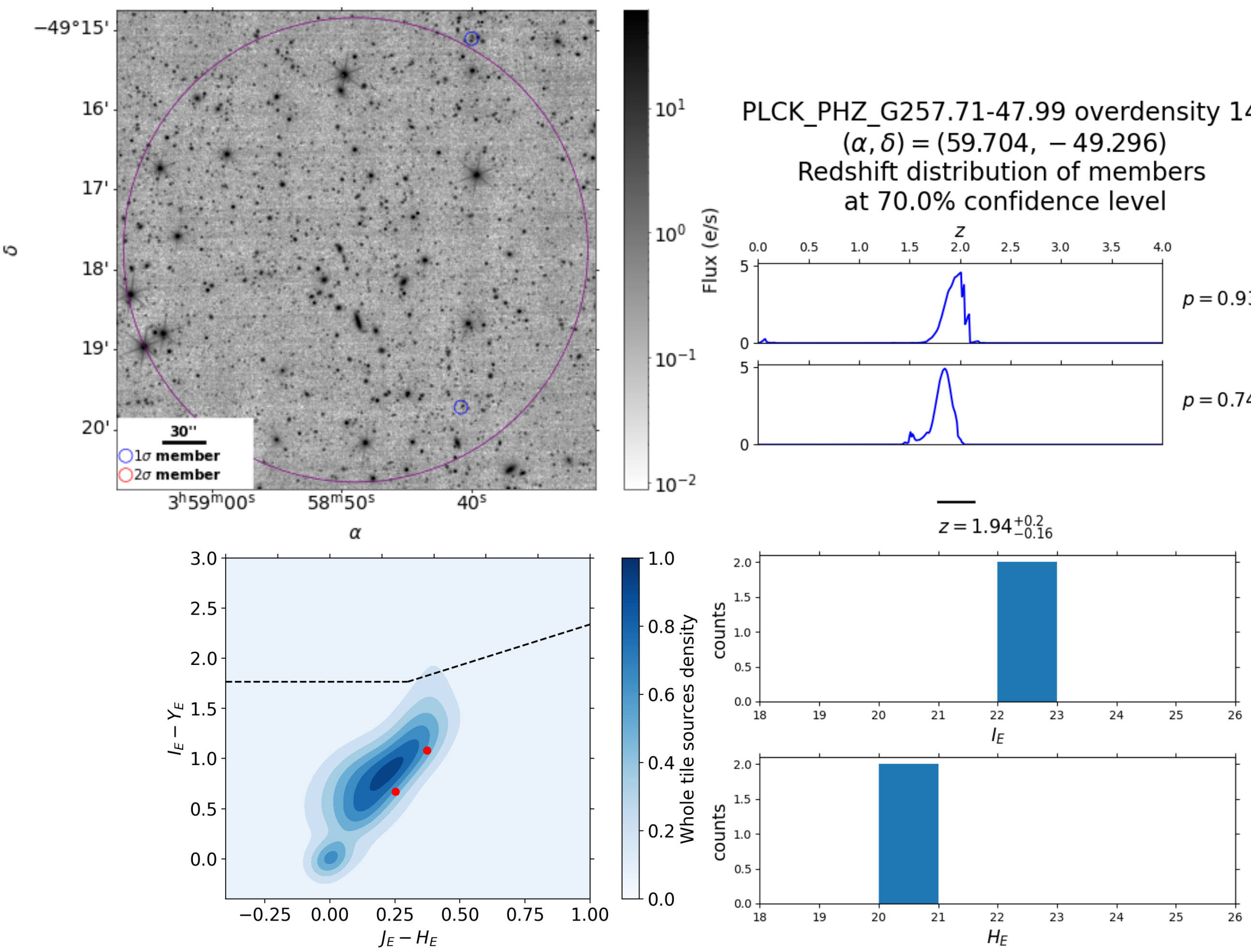

Fig. C.4. *Euclid* protocluster detected by DETECTIFz: NIR $H_{\rm E}$ image; Photometric redshifts; colour-colour plot; histograms of VIS $I_{\rm E}$ and NIR $H_{\rm E}$ magnitudes.